

# Isothermal transport of a near-critical binary fluid mixture through a capillary tube with the preferential adsorption

Shunsuke Yabunaka\*

*Department of Physics, Kyushu University, Fukuoka 819-0395, Japan*

Youhei Fujitani<sup>†</sup>

*School of Fundamental Science and Technology,*

*Keio University, Yokohama 223-8522, Japan*

(Dated: May 4, 2021)

## Abstract

We study isothermal transport of a binary fluid mixture in the homogeneous phase near the demixing critical point through a capillary tube connecting two reservoirs. It is usual that one component is preferentially adsorbed by the tube wall, and its influence is amplified because of the near-criticality. We consider the resultant inhomogeneous composition in terms of the renormalized local functional theory, which was previously devised to explain the interaction between two plates immersed in a near-critical binary fluid mixture. The inhomogeneity causes that of the correlation length, and then that of the transport coefficients. How the mass flow rates of the components through the tube depend on the temperature cannot be explained by the critical enhancement of the transport coefficients because of the off-critical composition in the tube. Deriving formulae of the Onsager coefficients, we numerically calculate the mass flow rates for a mixture of 2,6-lutidine and water and for a mixture of nitroethane and 3-methylpentane. When the flow is driven by pressure difference between the reservoirs, the composition of the mixture flowing out of the tube is modified by the preferential adsorption. When the flow is driven by mass-fraction difference, the total mass flow rate is raised distinctly by convection emerging in the presence of the preferential adsorption. These phenomena can be regarded as representing cross effects linked with each other via the reciprocal relation.

PACS numbers:

---

\*yabunaka123@gmail.com

†E-mail address: youhei@appi.keio.ac.jp

## I. INTRODUCTION

In a binary fluid mixture in the homogeneous phase close to the demixing critical point, we can study a flow, whose typical length scale is larger than the correlation length of the composition fluctuation, in terms of the hydrodynamics without thermal noise, because the critical fluctuation occurs on smaller length scales[1, 2]. The transport coefficients are enhanced by the fluctuation and depend on the correlation length[3, 4]. At the equilibrium, the coarse-grained composition is homogeneous in the bulk of a mixture, but can be inhomogeneous near an interface because one component can be preferentially attracted by another material, such as inner surface of the container[5–10]. We assume that the preferential adsorption arises from a short-range interaction, such as the hydrogen bond. Still, the adsorption layer, where the preferblack component is more concentrated, can be significantly thick in a near-critical mixture because of its large susceptibility. The inhomogeneity of the composition is linked with that of the correlation length. The former can generate additional hydrodynamic stress, while the latter causes that of each transport coefficient, in the dynamics.

The free-energy functional coarse-grained up to the local correlation length is obtained in the renormalized local functional theory[11, 12]. The equilibrium profile of the coarse-grained composition, or that of the order parameter, in a near-critical binary fluid mixture between parallel walls is calculated by minimizing the coarse-grained free-energy functional[12]. The hydrodynamics can be formulated from the free-energy functional[13], and thus can be based on the renormalized local functional theory[14, 15]. In particular, the drag coefficient of a colloidal particle in a near-critical binary fluid mixture is calculated in this framework[16]. One component is preferentially attracted by the particle surface. The drag force partly comes from the deformation of the adsorption layer caused by the particle motion, and the inhomogeneity of the correlation length is shown to be significant for the dependence of the drag coefficient on the temperature.

Much attention has been paid on flow through a channel in the field of soft matter physics[17–22]. In the present study, we consider isothermal transport of a binary fluid mixture in the homogeneous phase near the demixing critical point through a capillary

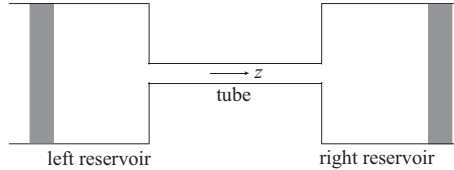


FIG. 1: A capillary tube connects the two reservoirs. A quantity in the right (left) reservoir is indicated with the subscript  $R$  ( $L$ ). Each of the thick walls represents a piston, which is installed to drive flow through the tube. The  $z$  axis is taken along the cylindrical tube in Sect. III.

tube connecting two sufficiently large reservoirs. A weak flow is assumed to be generated by imposed differences in pressure and mass fraction between the reservoirs, with the mixture remaining in the homogeneous phase. The temporal changes of the differences, if any, are assumed to be sufficiently small. We calculate the Onsager coefficients of the transport by considering a weak stationary laminar flow in the tube by using the hydrodynamics[23]. Assuming the tube to be cylindrical and setting the reference composition equal to the critical one, we study the dependence of the coefficients on the temperature. The tube radius is assumed to be so small that the adsorption layer is not negligible but is so large that the no-slip boundary condition can be imposed in the hydrodynamics. The tube length is assumed to be so large that effects of the flow near the tube edges are negligible. The inhomogeneity of the correlation length is taken into account, unlike in the previous studies on similar situations[24–26].

We review a framework for the Onsager coefficients in Sect. IIA and formulate the hydrodynamics in Sect. IIB. The pressure felt by the piston depends on the composition, or the mass fraction, of the binary fluid mixture in the reservoir. We derive formulae of the coefficients for a cylindrical tube in Sect. III, not assuming the mass density of the mixture to be homogeneous at the equilibrium. It can be shown that the formulae satisfy Onsager’s reciprocal relation[27, 28]. In Sect. IV, we apply the renormalized local functional theory to the formulae. It is assumed in this application that the mass density of the mixture is homogeneous at the equilibrium and that the mixture has the critical composition in the reference state. Using some previous experimental results for the material constants, we numerically calculate the Onsager coefficients for a mixture of 2,6-lutidine and water (LW) and a mixture of nitroethane and 3-methylpentane (NEMP) in Sect. V. The last section is

devoted to the discussion.

## II. FORMULATION

The mixture components are referred to as a and b. We write  $\rho_n$  for the mass density of the component  $n$  ( $n = a$  or  $b$ ), and  $\mu_n$  for the chemical potential conjugate to  $\rho_n$ , *i.e.*,  $\mu_n$  is the Gibbs free-energy per unit mass of the component  $n$ . In the bulk of an equilibrium mixture,  $\mu_n$  is a function of the temperature (denoted by  $T$ ), pressure ( $P$ ), and mass fraction of the component  $a$  ( $c_a$ ). That of the component  $b$ ,  $c_b$ , equals  $1 - c_a$ . We write  $\mu_{\pm}$  for  $(\mu_a \pm \mu_b)/2$ , and define  $\mu$  as the deviation of  $\mu_-$  from its value at the critical point. With the subscript  $c$  indicating the value at the critical point,  $\mu \equiv \mu_- - (\mu_-)_c$  vanishes at the critical point. We write  $\rho$  and  $\varphi$  for  $\rho_a + \rho_b$  and  $\rho_a - \rho_b$ , respectively;  $\rho$  and  $\varphi$  are conjugate to  $\mu_+$  and  $\mu_-$ , respectively. A quantity in each reservoir is indicated with the subscript  $R$  or  $L$ ;  $\mathcal{M}_{nR}$  denotes the total mass of the component  $n$  in the right reservoir of Fig. 1. The tube is not necessarily cylindrical in this section.

### A. Onsager coefficients

We first consider the entropy production rate of the mixture in the fluctuation about the equilibrium in the isolated container, which is composed of a capillary tube and two large reservoirs. Even at the equilibrium, a physical quantity fluctuates around its equilibrium value on length and time scales smaller than macroscopic ones. We write  $S$  for the total entropy of the mixture and  $t$  for the time. Neglecting the contribution from the mixture in the tube, we find the entropy production rate of the mixture in the container to be given by

$$\frac{dS}{dt} = - \sum_{n=a,b} \frac{\mu_{nR} - \mu_{nL}}{T} \frac{d\mathcal{M}_{nR}}{dt} \quad (1)$$

up to the second order of the magnitudes of the deviations. Here, we drop the terms which do not affect our following discussion on the isothermal transport of a mixture without chemical reactions. Equation (1) are thus consistent with Eq. (XV-55) of Ref. [23]. The thermodynamic force,  $(\mu_{nR} - \mu_{nL})/T$ , is equal to  $\partial S/(\partial \mathcal{M}_{nR})$ , where  $S$  is regarded as a function of  $\mathcal{M}_{aR}$ ,  $\mathcal{M}_{bR}$ , and the internal energy of the mixture in the right reservoir.

We rewrite Eq. (1) for later convenience. Writing  $g$  for the Gibbs free-energy per unit mass, we have  $dg = (dP/\rho) + 2\mu_-dc_a$  under  $dT = 0$  in the bulk of an equilibrium mixture, with  $d$  indicating the total derivative. We use  $\delta$  to indicate the difference of the value of a quantity in the central (or bulk) region of the left reservoir subtracted from that of the right reservoir. Because  $\mu_-$  equals half the partial derivative of  $g$  with respect to  $c_a$  with  $T$  and  $P$  being fixed, we can use

$$\delta\mu_- = \frac{1}{2} \left. \frac{\partial\rho^{-1}}{\partial c_a} \right)_{T,P} \delta P + \left. \frac{\partial\mu_-}{\partial c_a} \right)_{T,P} \delta c_a, \quad (2)$$

where the subscript  $T,P$  indicate the fixed variables in the partial differentiation and the partial derivatives are evaluated in the central region of the reservoir at the equilibrium. We can replace  $\mu_-$  by  $\mu$  in Eq. (2); the second term on the right-hand side represents the part of  $\delta\mu$  caused by  $\delta c_a$  and is denoted by  $(\delta\mu)_P$ . We write  $\bar{v}_a$  ( $\bar{v}_b$ ) for the partial volume per unit mass of the component a (b), which is defined as the partial derivative of the volume of the mixture with respect to the mass of the component a (b) with  $T$ ,  $P$ , and the mass of the other component being fixed. We have

$$1 = \bar{v}_a\rho_a + \bar{v}_b\rho_b = \frac{1}{2} [\rho(\bar{v}_a + \bar{v}_b) + \varphi(\bar{v}_a - \bar{v}_b)] \quad (3)$$

in the bulk of an equilibrium mixture. The partial derivative in the first term on the right-hand side of Eq. (2) equals  $\bar{v}_a^{(\text{eq})} - \bar{v}_b^{(\text{eq})}$ , which is  $\bar{v}_a - \bar{v}_b$  evaluated in the central region of the reservoir at the equilibrium. The superscript  $(\text{eq})$  is used to indicate the equilibrium value in this region. Equation (2) is thus rewritten as

$$\delta\mu = \bar{v}_-^{(\text{eq})} \delta P + (\delta\mu)_P, \quad (4)$$

where  $\bar{v}_-^{(\text{eq})}$  is defined as  $(\bar{v}_a^{(\text{eq})} - \bar{v}_b^{(\text{eq})})/2$ . With the aid of the Gibbs-Duhem relation for  $dT = 0$ ,  $dP/\rho = c_a d\mu_a + c_b d\mu_b$ , we use Eqs. (3) and (4) to rewrite Eq. (1) as

$$\frac{dS}{dt} = -\frac{\delta P}{T} \frac{d\alpha_1}{dt} - \frac{(\delta\mu)_P}{T} \frac{d\alpha_2}{dt}, \quad (5)$$

where  $\alpha_1$  and  $\alpha_2$  are defined as

$$\begin{pmatrix} \alpha_1 \\ \alpha_2 \end{pmatrix} = \begin{pmatrix} \bar{v}_a^{(\text{eq})} & \bar{v}_b^{(\text{eq})} \\ 2c_b^{(\text{eq})} & -2c_a^{(\text{eq})} \end{pmatrix} \begin{pmatrix} \mathcal{M}_{\text{aR}} \\ \mathcal{M}_{\text{bR}} \end{pmatrix}. \quad (6)$$

Here,  $c_n^{(\text{eq})}$  denotes the value of  $c_n$  in the central region of the reservoir at the equilibrium. We write  $I$  and  $J$  for new thermodynamic fluxes  $d\alpha_1/(dt)$  and  $d\alpha_2/(dt)$ , respectively. New

thermodynamic forces conjugate to them are, respectively, given by  $\partial S/(\partial\alpha_1) = -\delta P/T$  and  $\partial S/(\partial\alpha_2) = -(\delta\mu)_P/T$ .

Hereafter, we discuss macroscopic descriptions of a mixture. In the non-equilibrium thermodynamics for the isothermal transport caused by weak external thermodynamic forces, we assume linear relationship between the thermodynamic fluxes and forces, which appear in the equations mentioned above[27, 28]. The linear phenomenological equations based on Eq. (5) are represented by[23]

$$\begin{pmatrix} I \\ J \end{pmatrix} = \mathcal{K} \begin{pmatrix} -\delta P/T \\ -(\delta\mu)_P/T \end{pmatrix}, \quad (7)$$

where  $\mathcal{K}$  is a  $2 \times 2$  matrix. Its components are Onsager coefficients, which should satisfy  $\mathcal{K}_{11}\mathcal{K}_{22} - \mathcal{K}_{12}^2 > 0, \mathcal{K}_{11} > 0, \mathcal{K}_{22} > 0$ , and  $\mathcal{K}_{12} = \mathcal{K}_{21}$ . The last represents Onsager's reciprocal relation. Macroscopically, an equilibrium mixture fluid has homogeneous chemical potentials. Even in the presence of flow in the tube, the mixture is regarded as being at the equilibrium in the reservoir, except in the immediate vicinity of the tube edge. In each reservoir, because of the mechanical balance, the pressure felt by the piston in Fig. 1 is always the same as the pressure in the central region, where the mass densities are always regarded as homogeneous. Thus,  $\delta P$  equals the difference in the pressure felt by the piston between the reservoirs, and thus can be controlled externally.

## B. Hydrodynamics

We can formulate the hydrodynamics by using the Helmholtz free-energy for coarse-grained fields. The fields mentioned below have been coarse-grained up to the local correlation length. Considering that the mass densities can depend on the position  $\mathbf{r}$ , we assume the free energy of the mixture bulk to be given by the volume integral of a function of  $\rho_a, \rho_b$  and the quadratic form of their gradients over the mixture region,  $V_{\text{tot}}$ . To describe the preferential attraction due to a short-range interaction, we add the surface integral of a function of  $\rho_a$  and  $\rho_b$ , or  $\rho$  and  $\varphi$ , over the interface between the mixture and the container,  $\partial V_{\text{tot}}$ . With  $f_{\text{bulk}}$  and  $f_{\text{surf}}$  denoting these functions, respectively, the free-energy functional

is given by

$$\mathcal{F}[\rho_a, \rho_b] = \int_{V_{\text{tot}}} d\mathbf{r} f_{\text{bulk}}(\rho, \varphi, \nabla\rho, \nabla\varphi) + \int_{\partial V_{\text{tot}}} dA f_{\text{surf}}(\rho, \varphi) . \quad (8)$$

The variables of  $f_{\text{bulk}}$  are written as above for later convenience, although it depends on the gradients only through  $|\nabla\rho_a|^2$ ,  $|\nabla\rho_b|^2$ , and  $(\nabla\rho_a) \cdot (\nabla\rho_b)$ . In the dynamics, deviations of the mass densities from their equilibrium values lead to inhomogeneous chemical potentials. In general,  $\mu_n(\mathbf{r})$  is given by the functional derivative of  $\mathcal{F}[\rho_a, \rho_b]$  with respect to  $\rho_n(\mathbf{r})$  in the mixture bulk. We thus have

$$\mu_+ = \frac{\partial f_{\text{bulk}}}{\partial \rho} - \nabla \cdot \left( \frac{\partial f_{\text{bulk}}}{\partial \nabla \rho} \right) \quad \text{and} \quad \mu_- = \frac{\partial f_{\text{bulk}}}{\partial \varphi} - \nabla \cdot \left( \frac{\partial f_{\text{bulk}}}{\partial \nabla \varphi} \right) , \quad (9)$$

which are homogeneous at the equilibrium. We can obtain the reversible part of the pressure tensor,  $\Pi_{\text{rev}}$ , by considering the change of the free energy generated by a quasistatic deformation of a mixture. Its scalar part,  $P$ , equals the negative of the grand-potential density, *i.e.*,

$$P = -f_{\text{bulk}} + \rho_a \mu_a + \rho_b \mu_b = -f_{\text{bulk}} + \rho \mu_+ + \varphi \mu_- . \quad (10)$$

As shown in Appendix A, with  $\mathbf{1}$  denoting the isotropic tensor, we have

$$\Pi_{\text{rev}} = P\mathbf{1} + \frac{\partial f_{\text{bulk}}}{\partial (\nabla \rho)} (\nabla \rho) + \frac{\partial f_{\text{bulk}}}{\partial (\nabla \varphi)} (\nabla \varphi) , \quad (11)$$

which is a symmetric tensor. After some algebra, we obtain

$$\nabla \cdot \Pi_{\text{rev}} = \rho \nabla \mu_+ + \varphi \nabla \mu_- . \quad (12)$$

Because of the homogeneous densities in the central region of each reservoir, we use Eqs. (9) and (10) to find that the pressure difference appearing in Eq. (7) is given by

$$\delta P = \rho^{(\text{eq})} \delta \mu_+ + \varphi^{(\text{eq})} \delta \mu_- , \quad (13)$$

where  $\rho^{(\text{eq})}$  and  $\varphi^{(\text{eq})}$  denote the values of  $\rho$  and  $\varphi$ , respectively, in the central region at the equilibrium. Considering Eq. (4),  $\delta \mu_+$  is thus determined by  $\delta P$  and  $\delta c_a$ .

The diffusion fluxes of the components a and b are respectively denoted by  $\mathbf{j}_a$  and  $\mathbf{j}_b$ . Their sum vanishes, while the difference,  $\mathbf{j}_a - \mathbf{j}_b$ , is denoted by  $\mathbf{j}$ . The mass conservation of component  $n(= a \text{ or } b)$  is represented by

$$\frac{\partial \rho_n}{\partial t} = -\nabla \cdot (\rho_n \mathbf{v}) - \nabla \cdot \mathbf{j}_n . \quad (14)$$



The sum over  $n = a$  and  $b$  is

$$\frac{\partial \rho}{\partial t} = -\nabla \cdot (\rho \mathbf{v}) , \quad (15)$$

while the difference gives

$$\frac{\partial \varphi}{\partial t} = -\nabla \cdot (\varphi \mathbf{v}) - \nabla \cdot \mathbf{j} , \quad (16)$$

which describes the interdiffusion of the components. We can assume  $\mathbf{j}$  to be equal to  $-\Lambda \nabla \mu$ , where  $\Lambda$  denotes the transport coefficient for the interdiffusion. The container's inner surface is assumed to be impermeable to the mixture, which means that the normal component of  $\nabla \mu$  vanishes at  $\partial V_{\text{tot}}$ . As mentioned later, in a weak stationary laminar flow in the tube we consider,  $\nabla \cdot \mathbf{v} = 0$  is valid although  $\rho$  is not assumed to be constant. Thus, the momentum conservation gives

$$0 = -\rho \nabla \mu_+ - \varphi \nabla \mu + 2\nabla \cdot (\eta_s E) , \quad (17)$$

where  $\eta_s$  is the shear viscosity and  $E$  the rate-of-strain tensor. The no-slip boundary condition is imposed at  $\partial V_{\text{tot}}$ . As mentioned in Sect. I, the transport coefficients,  $\eta_s$  and  $\Lambda$ , can be inhomogeneous. The left-hand sides of Eqs. (14) - (16) vanish in the stationary state.

The mass densities at the equilibrium minimize

$$\mathcal{F}[\rho_a, \rho_b] - \int_{V_{\text{tot}}} d\mathbf{r} [\mu_a \rho_a(\mathbf{r}) + \mu_b \rho_b(\mathbf{r})] , \quad (18)$$

because the fields are coarse-grained up to the local correlation length. Thus, the mass densities satisfy the two equations in Eq. (9) with their left-hand sides determined by the homogeneous chemical potentials set in Eq. (18), together with the boundary conditions

$$\mathbf{n}_{\partial V_{\text{tot}}} \cdot \frac{\partial f_{\text{bulk}}}{\partial (\nabla \rho)} + \frac{\partial f_{\text{surf}}}{\partial \rho} = \mathbf{n}_{\partial V_{\text{tot}}} \cdot \frac{\partial f_{\text{bulk}}}{\partial (\nabla \varphi)} + \frac{\partial f_{\text{surf}}}{\partial \varphi} = 0 \quad \text{at } \partial V_{\text{tot}} , \quad (19)$$

where  $\mathbf{n}_{\partial V_{\text{tot}}}$  denotes the outward facing unit vector normal to  $\partial V_{\text{tot}}$ . Homogeneous chemical potentials imply the mechanical balance at the equilibrium,  $\nabla \cdot \Pi_{\text{rev}} = 0$ , because of Eq. (12). We note that Eq. (3) need not hold in a region with inhomogeneous mass densities.

### III. SOLUTION OF THE DYNAMIC EQUATIONS

Through a cylindrical tube, with the radius  $r_{\text{tube}}$ , a stationary laminar flow is assumed to be driven by a nonzero small values of  $|\delta P|$  and  $|(\delta \mu)_P|$ . Assuming that  $\delta P$  and  $(\delta \mu)_P$  are

proportional to a dimensionless smallness parameter,  $\varepsilon$ , we calculate the fields in the tube up to the order of  $\varepsilon$  to obtain the Onsager coefficients. The superscripts  $(0)$  and  $(1)$  indicate the order of  $\varepsilon$ . For example, we have  $\mu_+ = \mu_+^{(0)} + \varepsilon\mu_+^{(1)}$  up to the order of  $\varepsilon$ . In this notation, we replace  $\mu_a$  and  $\mu_b$  by  $\mu_+^{(0)} + \mu_-^{(0)}$  and  $\mu_+^{(0)} - \mu_-^{(0)}$  in Eq. (18), respectively, to calculate the equilibrium mass densities. As mentioned in the preface of Sect. II,  $\mu_{\pm}^{(0)}$  are homogeneous and equal to  $\mu_{\pm}^{(\text{eq})}$ , respectively. In the tube, the equilibrium mass densities are functions of the distance from the center axis ( $z$  axis in Fig. 1), and are denoted by  $\rho^{(0)}(r)$  and  $\varphi^{(0)}(r)$  with  $r$  denoting the distance. The transport coefficients can be regarded as dependent on these mass densities for  $\varepsilon = 0$  in the dynamic equations up to the order of  $\varepsilon$ . The resultant  $r$ -dependent viscosity and transport coefficient for the interdiffusion are denoted by  $\eta_0(r)$  and  $\Lambda_0(r)$ , respectively. We note that, if  $\rho$  and  $\varphi$  are homogeneous, Eq. (12) becomes  $\nabla P$ . Then, with the homogeneous transport coefficients, we have the usual Hagen-Poiseuille flow with the interdiffusion. The preferential adsorption breaks the homogeneity.

### A. Velocity field

We take the Cartesian coordinate system  $(x, y, z)$  in the tube so that the right reservoir is on the positive side of  $z$ . A laminar flow is assumed in the tube;  $\mathbf{v}$  is along the  $z$  axis. Because of  $\mathbf{v}^{(0)} = \mathbf{0}$ , Eq. (15) in the stationary state gives

$$0 = \nabla \cdot \mathbf{v}^{(1)} = \partial_z v_z^{(1)} , \quad (20)$$

where  $\partial_z$  denotes the partial derivative with respect to  $z$ . The  $x$  and  $y$  components of Eq. (17) give

$$0 = \rho^{(0)} \partial_r \mu_+^{(1)} + \varphi^{(0)} \partial_r \mu^{(1)} \quad (21)$$

because of the axial symmetry. The  $z$  component of Eq. (17) gives

$$\partial_z \left( \rho^{(0)} \mu_+^{(1)} + \varphi^{(0)} \mu^{(1)} \right) = \frac{1}{r} \partial_r \left( r \eta_0(r) \partial_r v_z^{(1)} \right) , \quad (22)$$

which is differentiated with respect to  $z$  to yield

$$0 = \rho^{(0)} \partial_z^2 \mu_+^{(1)} + \varphi^{(0)} \partial_z^2 \mu^{(1)} . \quad (23)$$

This means that functions  $Q_1(r)$  and  $Q_0(r)$  can be defined so that

$$\rho^{(0)} \mu_+^{(1)} + \varphi^{(0)} \mu^{(1)} = Q_1(r)z + Q_0(r) \quad (24)$$

holds. Subtracting Eq. (21) from the partial derivative of Eq. (24) with respect to  $r$ , and differentiating the resultant difference with respect to  $z$  twice, we obtain

$$0 = \rho^{(0)'} \partial_z^2 \mu_+^{(1)} + \varphi^{(0)'} \partial_z^2 \mu^{(1)} , \quad (25)$$

where the prime indicates the derivative with respect to the variable. Equations (23) and (25) in general mean  $\partial_z^2 \mu_+^{(1)} = \partial_z^2 \mu^{(1)} = 0$ . Because of Eq. (16), we thus find  $\partial_r (r \Lambda_0 \partial_r \mu^{(1)})$  to vanish. Combining this differential equation for  $\partial_r \mu^{(1)}$  with the boundary condition mentioned below Eq. (16), we find that  $\mu^{(1)}$  is a linear function of  $z$  and is independent of  $x$  and  $y$ . Hence, because of Eqs. (21) and (23), we also find that  $\mu_+^{(1)}$  is a linear function of  $z$  and is independent of  $x$  and  $y$ . Neglecting the flow near the tube edge in the reservoir, we regard  $\delta \mu_+^{(1)}$  and  $\delta \mu^{(1)}$  as giving the differences in  $\mu_+^{(1)}$  and  $\mu^{(1)}$  between the tube edges, respectively. This approximation is consistent with the independence of  $\mu^{(1)}$  from  $x$  and  $y$  in the tube. Writing  $L_{\text{tube}}$  for the length of the tube, because of Eq. (13), we have

$$\varepsilon \partial_z \mu_+^{(1)} = \frac{\delta P - \varphi^{(\text{eq})} \delta \mu}{\rho^{(\text{eq})} L_{\text{tube}}} \quad \text{and} \quad \varepsilon \partial_z \mu^{(1)} = \frac{\delta \mu}{L_{\text{tube}}} . \quad (26)$$

These results hold on the assumption above even if the tube is not cylindrical, as far as  $\rho^{(0)}$  and  $\varphi^{(0)}$  are independent of  $z$ .

Because of the no-slip condition and the axisymmetry of flow, respectively,  $v_z^{(1)}$  vanishes at  $r = r_{\text{tube}}$  and  $\partial_r v_z$  vanishes at  $r = 0$ . Equation (22) gives

$$v_z^{(1)}(r) = - \int_r^{r_{\text{tube}}} ds' \frac{1}{s' \eta_0(s')} \int_0^{s'} ds s \left( \rho^{(0)} \partial_z \mu_+^{(1)} + \varphi^{(0)}(s) \partial_z \mu^{(1)} \right) , \quad (27)$$

into which Eq. (26) is substituted to give

$$\begin{aligned} \varepsilon v_z^{(1)}(r) = & - \frac{\delta P}{L_{\text{tube}}} \int_r^{r_{\text{tube}}} ds' \frac{1}{s' \eta_0(s')} \int_0^{s'} ds s \frac{\rho^{(0)}}{\rho^{(\text{eq})}} \\ & - \frac{\delta \mu}{L_{\text{tube}}} \int_r^{r_{\text{tube}}} ds' \frac{1}{s' \eta_0(s')} \int_0^{s'} ds s \left( \varphi^{(0)} - \frac{\rho^{(0)} \varphi^{(\text{eq})}}{\rho^{(\text{eq})}} \right) . \end{aligned} \quad (28)$$

Owing to  $\mathbf{j}^{(1)} = -\Lambda_0 \nabla \mu^{(1)}$ ,  $\mathbf{j}^{(1)}$  is along the  $z$  axis. Thus,  $\mathbf{j}_a^{(1)} = -\mathbf{j}_b^{(1)}$  is also along the  $z$  axis, and we have

$$\varepsilon j_z^{(1)}(r) = -\Lambda_0(r) \frac{\delta \mu}{L_{\text{tube}}} . \quad (29)$$

In the absence of the preferential adsorption, because of  $\rho^{(0)}(r) = \rho^{(\text{eq})}$  and  $\varphi^{(0)}(r) = \varphi^{(\text{eq})}$ ,  $\eta_0$  is a constant and the sum in the parentheses of Eq. (27) equals  $\partial_z P$ , which leads to the usual Hagen-Poiseuille flow.

## B. Onsager coefficients

Equations (28) and (29) relate  $v_z^{(1)}$  and  $j_z^{(1)}$  with  $\delta P/T$  and  $\delta\mu/T$ . Equation (4) links this set of thermodynamic forces with the set in Eq. (7) as

$$\begin{pmatrix} -\delta P/T \\ -(\delta\mu)_P/T \end{pmatrix} = \begin{pmatrix} 1 & 0 \\ -\bar{v}_-^{(\text{eq})} & 1 \end{pmatrix} \begin{pmatrix} -\delta P/T \\ -\delta\mu/T \end{pmatrix}. \quad (30)$$

The first matrix on the right-hand side above is denoted by  $N$ , and becomes the identity matrix when  $\bar{v}_-^{(\text{eq})}$  vanishes. The thermodynamic fluxes conjugate to  $-\delta P/T$  and  $-\delta\mu/T$ , denoted by  $\mathcal{I}$  and  $\mathcal{J}$ , are

$$\begin{pmatrix} \mathcal{I} \\ \mathcal{J} \end{pmatrix} = N^T \begin{pmatrix} I \\ J \end{pmatrix} \quad (31)$$

with the superscript  $T$  indicating the transposition, and thus  $\mathcal{J}$  equals  $J$ . Up to the order of  $\varepsilon$ , the mass flow rate of the component  $n$  into the right reservoir is given by

$$\frac{d}{dt}\mathcal{M}_{nR} = \varepsilon \int_{S_{\text{tube}}} dA (\rho_n^{(0)}v_z^{(1)} + j_{nz}^{(1)}), \quad (32)$$

whose right-hand side represents the area integral of the mass flux of the component  $n$  over a cross-sectional disk of the tube,  $S_{\text{tube}}$ . The sum of Eq. (32) over  $n = a$  and  $b$  gives the rate of the total mass flow into the right reservoir. With the aid of Eq. (3), we use Eqs. (6), (31), and (32) to obtain

$$\mathcal{I} = \frac{\varepsilon}{\rho^{(\text{eq})}} \int_{S_{\text{tube}}} dA \rho^{(0)}v_z^{(1)} \quad (33)$$

$$\text{and } \mathcal{J} = \varepsilon \int_{S_{\text{tube}}} dA \left[ \left( \varphi^{(0)} - \frac{\rho^{(0)}\varphi^{(\text{eq})}}{\rho^{(\text{eq})}} \right) v_z^{(1)} + j_z^{(1)} \right] \quad (34)$$

up to the order of  $\varepsilon$ . Because of Eqs. (15) and (16),  $\mathcal{I}$  is the total mass flow rate divided by  $\rho^{(\text{eq})}$ , while  $\mathcal{J} + \varphi^{(\text{eq})}\mathcal{I}$  is the difference of the mass flow rate of the component  $b$  into the right reservoir subtracted from that of the component  $a$ . The linear phenomenological equations can be written as

$$\begin{pmatrix} \mathcal{I} \\ \mathcal{J} \end{pmatrix} = \mathcal{L} \begin{pmatrix} -\delta P/T \\ -\delta\mu/T \end{pmatrix}, \quad (35)$$

where  $\mathcal{L}$  is defined as  $N^T\mathcal{K}N$ . The components of  $\mathcal{L}$  are also Onsager coefficients. In Appendix B, even if the tube is not cylindrical, our formulation up to here is shown to be

consistent with the reciprocal relations,  $\mathcal{L}_{12} = \mathcal{L}_{21}$  and  $\mathcal{K}_{12} = \mathcal{K}_{21}$ , as far as  $\rho^{(0)}$  and  $\varphi^{(0)}$  are independent of  $z$ .

We consider a transport through a cylindrical tube; the area integral over  $S_{\text{tube}}$  is represented by the integral with respect to  $r$  from  $r = 0$  to  $r_{\text{tube}}$  with the Jacobian being  $4\pi r^2$ . Substituting Eqs. (28) and (29) into Eqs. (33) and (34), we can write the components of  $\mathcal{L}$  for a cylindrical tube in terms of the integrals with respect to  $r$ . We find that the components  $\mathcal{L}_{11}$  and  $\mathcal{L}_{12} = \mathcal{L}_{21}$  depend on  $v_z^{(1)}$ , which means that they are involved in the convection, by noting that Eq. (33) and the first term in the brackets of Eq. (34) contain  $v_z^{(1)}$ . Part of the first term in the brackets, as well as the second term involved in the interdiffusion, contribute to  $\mathcal{L}_{22}$ . We refer to the parts of  $\mathcal{L}_{22}$  coming from them as  $\mathcal{L}_{22v}$  and  $\mathcal{L}_{22d}$ , respectively. In the absence of the preferential adsorption,  $\rho^{(0)}(r) = \rho^{(\text{eq})}$  and  $\varphi^{(0)}(r) = \varphi^{(\text{eq})}$  make the difference in the parentheses of Eq. (34) vanish. This means  $\mathcal{L}_{21} = 0$  and  $\mathcal{L}_{22v} = 0$ . Owing to the reciprocal relation, the former gives  $\mathcal{L}_{12} = 0$ , which we can derive alternatively by noting that the same difference appears in the parentheses of Eq. (28).

With the aid of Eqs. (33) and (34), we can rewrite Eq. (32) as

$$\frac{d}{dt}\mathcal{M}_{nR} = \rho_n^{(\text{eq})}\mathcal{I} \pm \frac{1}{2}\mathcal{J}, \quad (36)$$

where the upper (lower) sign is taken for  $n = a$  (b) in the double sign. The first term on the right-hand side above is proportional to  $c_n^{(\text{eq})}$  and contributes to the total mass flow rate, which is not changed by the second term. Equation (35) can be substituted into  $\mathcal{I}$  and  $\mathcal{J}$  above. In the absence of the preferential adsorption, the first term on the right-hand side of Eq. (36) is blackuced to  $-\rho_n^{(\text{eq})}\mathcal{L}_{11}\delta P/T$ , while the second term to  $\mp\mathcal{L}_{22d}\delta\mu/(2T)$ . They are involved in the convection and interdiffusion, respectively. Thus, in the absence, when a flow is driven by pressure difference, *i.e.*, by  $\delta P \neq 0$  and  $\delta c_a = 0$ , the convected part of the mixture has the mass fraction of  $c_n^{(\text{eq})}$ . Then, unless  $\bar{v}_-^{(\text{eq})}$  vanishes, the interdiffusion occurs in addition to alter the mass fraction of a mixture flowing out of the tube per unit time from  $c_n^{(\text{eq})}$ . In the absence, only the interdiffusion occurs when a flow is driven by mass-fraction difference, *i.e.*, by  $\delta c_a \neq 0$  and  $\delta P = 0$ .

In the presence of the preferential adsorption,  $-\rho_n^{(\text{eq})}\mathcal{L}_{12}\delta\mu/T$  emerges in the first term on the

right-hand side of Eq. (36), while  $\mp \mathcal{L}_{21} \delta P / (2T)$  and  $\mp \mathcal{L}_{22v} \delta \mu / (2T)$  emerge in the second term. Because of the second of these emergent terms, when a flow is driven by pressure difference, even the convected part of the mixture does not have the mass fraction of  $c_n^{(\text{eq})}$ , which is realized considering that the preferblack component is concentrated in the tube. This is caused by the term involving  $\mathcal{L}_{21}$ . Because of the first and third of the emergent terms, not only the interdiffusion but also the convective transport occurs when a flow is driven by mass-fraction difference. In particular, the first term, involving  $\mathcal{L}_{12}$ , generates the total mass flow rate. The emergent terms involving  $\mathcal{L}_{21}$  and  $\mathcal{L}_{12}$  represent the cross effects in Eq. (35), and are related with each other via the reciprocal relation. The origin of the cross effects can be traced back to the reciprocal relation appearing between the reversible terms in Eqs. (14) and (17) after they are linearized, as mentioned at the end of Appendix A. The preferential adsorption also makes  $\mathcal{L}_{22v}$  emergent. This term is involved in generating the mass flow rates of the components, without changing the total rate, in a flow driven by mass-fraction difference, like the term for the interdiffusion.

#### IV. ELEMENTS FOR NUMERICAL CALCULATIONS

We assume that the mixture in the central regions of the reservoirs has the critical composition at the equilibrium. In other words, we assume  $\varphi^{(\text{eq})} = \varphi_c$ , where the subscript  $c$  indicates the critical value. The difference  $\varphi(\mathbf{r}) - \varphi_c$ , denoted by  $\psi(\mathbf{r})$ , is the order parameter of the phase separation. We also have  $\rho^{(\text{eq})} = \rho_c$  and  $\rho_n^{(\text{eq})} = \rho_{nc} = c_{ac} \rho^{(\text{eq})}$ . Some details requiblack for numerical calculations are specified in this section.

##### A. Free-energy functional

We assume that  $f_{\text{bulk}}$  is separated into  $\rho$ -dependent part and  $\psi$ -dependent part. Here, the former part is a function of  $\rho$ , denoted by  $f_+(\rho)$ , and the latter part consists of a function of  $\psi$ , denoted by  $f_-(\psi)$ , and the square gradient term. This term is denoted by  $M_-(\psi) |\nabla \psi|^2 / 2$  with  $M_-(\psi)$  representing a positive function of  $\psi$ . The expressions of  $f_-$  and  $M_-$  are given in terms of the renormalized local functional theory and mentioned in the next subsection. In this theory, as mentioned in Appendix C, the functional is obtained by coarse-graining

the Ginzburg-Landau-Wilson type of bare model, and assuming  $\varphi^{(\text{eq})} = \varphi_c$  amounts to assuming  $\mu_-^{(0)} = (\mu_-)_c$ , *i.e.*,  $\mu^{(0)} = 0$ . We also assume that  $f_{\text{surf}}$ , being independent of  $\rho$ , is proportional to  $\psi$  apart from a irrelevant constant. The negative of the constant of proportionality, denoted by  $h$ , is called the surface field[6, 29–31]. On these assumptions, Eq. (8) is replaced by

$$\mathcal{F}[\rho_a, \rho_b] = \int_{V_{\text{tot}}} d\mathbf{r} \left[ f_+(\rho) + f_-(\psi) + \frac{1}{2}M_-(\psi) |\nabla\psi|^2 \right] - h \int_{\partial V_{\text{tot}}} dA \psi . \quad (37)$$

Because of the statements in the last paragraph of Sect. IIB, we find that  $\rho^{(0)}$  is homogeneously equal to  $\rho^{(\text{eq})} = \rho_c$  and that  $\psi^{(0)}$  satisfies

$$h = M_-(\psi^{(0)}) \mathbf{n}_{\partial V_{\text{tot}}} \cdot \nabla \psi^{(0)} \quad \text{at } \partial V_{\text{tot}} , \quad (38)$$

which comes from Eq. (19), and

$$(\mu_-)_c = f'_-(\psi^{(0)}) - \frac{1}{2}M'_-(\psi^{(0)})|\nabla\psi^{(0)}|^2 - M_-(\psi^{(0)})\Delta\psi^{(0)} \quad \text{in } V_{\text{tot}} , \quad (39)$$

which comes from the second entry of Eq. (9). The equilibrium profile of the order parameter between the two parallel plates and the one around a sphere are calculated by solving Eq. (39) under the boundary condition given by Eq. (38)[11, 12, 16, 32–34].

Because  $\rho^{(0)}$  is homogeneous in Eq. (15) at the order of  $\varepsilon$ , we have  $\nabla \cdot \mathbf{v}^{(1)} = 0$  in a stationary flow, whether it is laminar or not. Equation (9) gives  $\mu_+ = f'_+(\rho)$  and thus  $\mu_+^{(1)} = \rho^{(1)} f''_+(\rho^{(0)})$ . Defining  $p$  as  $\rho f'_+ - f_+$ , we have  $p^{(1)} = \rho^{(0)} \mu_+^{(1)}$  to find Eq. (12) to become

$$\nabla \cdot \Pi_{\text{rev}}^{(1)} = \nabla p^{(1)} + \varphi^{(0)} \nabla \mu^{(1)} , \quad (40)$$

which is used in Ref. [16]. This previous reference supposes the incompressibility condition, which amounts to assuming  $|f''_+(\rho^{(0)})|$  to be sufficiently large. In the present study, we need not assume the mixture to be incompressible. In a mixture region with homogeneous densities, Eq. (10) gives  $P = p - f_- + \varphi \mu_-$  and thus Eq. (13) becomes

$$\delta P = \delta p + \varphi_c \delta \mu . \quad (41)$$

Because of  $\rho^{(0)} = \rho^{(\text{eq})}$  in Eq. (33),  $\mathcal{I}$  equals the area integral of  $\varepsilon v_z^{(1)}$  over  $S_{\text{tube}}$ , which gives the flow rate. We note that, even if  $\mathcal{I}$  vanishes, the diffusion fluxes can shift the composition in each reservoir to change its volume. The difference in the parentheses of Eq. (34) equals  $\psi^{(0)}$ .

## B. Non-dimensionalization

Using the conventional notation, we write  $\alpha, \beta, \gamma, \nu$ , and  $\eta$  for the critical exponents for binary mixtures near the demixing critical point (or in the three-dimensional Ising model). The values of the critical exponents are shown in Ref. [35]; we adopt  $\nu=0.630$  and  $\eta=0.0364$ . The exponent  $\eta$  represents the deviation from the straightforward dimensional analysis of the equal-time correlation function of the order-parameter fluctuation at the critical point. The critical temperature is denoted by  $T_c$ , and the blackuced temperature  $\tau$  is defined as  $|T - T_c|/T_c$ . In an equilibrium mixture with the critical composition ( $\psi = 0$ ), the correlation length, denoted by  $\xi$ , is given by  $\xi_0\tau^{-\nu}$  for small  $\tau$ , where  $\xi_0$  is a material constant. In general,  $\xi$  depends on  $\psi$  and  $\tau$ . The "distance" from the critical point is represented by  $\omega$ , which is defined so that we have

$$\xi = \xi_0\omega^{-\nu} . \quad (42)$$

We non-dimensionalize the equations to facilitate later numerical calculations. A dimensionless radial distance  $\hat{r}$  is defined as  $\hat{r} = r/r_{\text{tube}}$ . A characteristic blackuced temperature  $\tau_*$  is defined so that  $\xi$  becomes  $r_{\text{tube}}$  for  $\psi = 0$  at  $\tau = \tau_*$ . A characteristic order parameter  $\psi_*$  is defined so that  $\xi$  becomes  $r_{\text{tube}}$  for  $\psi = \psi_*$  at  $\tau = 0$ . According to Eq. (C4), these two definitions are equivalent to

$$\tau_* = \left( \frac{\xi_0}{r_{\text{tube}}} \right)^{1/\nu} \quad \text{and} \quad \psi_* = \frac{\tau_*^\beta}{\sqrt{C_2}} , \quad (43)$$

where  $C_2$  is a material constant. Its value can be estimated from the coexistence curve, as shown in Appendix D. We define  $\hat{\tau} \equiv \tau/\tau_*$ ,  $\hat{\omega} \equiv \omega/\tau_*$ , and  $\hat{\psi}^{(0)}(\hat{r}) \equiv \psi^{(0)}(r_{\text{tube}}\hat{r})/\psi_*$ , respectively. Defining a dimensionless function  $\hat{f}$  as

$$\hat{f}(\hat{\psi}) = \hat{\omega}^{\gamma-1}\hat{\tau} \left( \frac{\hat{\psi}^2}{2} + \frac{\hat{\psi}^4}{12\hat{\omega}^{2\beta-1}\hat{\tau}} \right) , \quad (44)$$

we have

$$f_-(\psi) - (\mu_-)_c\varphi = \frac{k_B T}{3u^*r_{\text{tube}}^3} \hat{f}(\hat{\psi}) , \quad (45)$$

which equals Eq. (C1) multiplied by  $k_B T$ . Here,  $k_B$  denotes the Boltzmann constant. We define  $\hat{\mu}$  as  $\mu/\mu_*$ , where  $\mu_*$  defined as

$$\mu_* = \frac{k_B T}{3u^*r_{\text{tube}}^3\psi_*} . \quad (46)$$



The dependence of  $\hat{\omega}$  on  $\hat{\psi}$  and  $\hat{\tau}$  is implicitly given by

$$\hat{\omega} = \hat{\tau} + \hat{\omega}^{1-2\beta} \hat{\psi}^2, \quad (47)$$

which is equivalent with Eq. (C4). Owing to Eqs. (38) and (39),  $\hat{\psi}^{(0)}(\hat{r})$  is the solution of the differential equation for  $\hat{\psi}(\hat{r})$ ,

$$0 = \hat{f}'(\hat{\psi}) - \frac{1}{2} \frac{d\hat{\omega}^{-\eta\nu}}{d\hat{\psi}} \left( \partial_{\hat{r}} \hat{\psi} \right)^2 - \hat{\omega}^{-\eta\nu} \left( \partial_{\hat{r}}^2 + \frac{1}{\hat{r}} \partial_{\hat{r}} \right) \hat{\psi} \quad \text{for } \hat{r} < 1, \quad (48)$$

together with the boundary condition

$$\partial_{\hat{r}} \hat{\psi} = \hat{h} \hat{\omega}^{\eta\nu} \quad \text{at } \hat{r} = 1, \quad (49)$$

where  $\hat{h}$  is a dimensionless surface field defined as  $\hat{h} = h / (\mu_* r_{\text{tube}})$ . A characteristic pressure is defined as  $\mu_* \psi_*$ ; we introduce dimensionless quantities corresponding to  $\delta P$  and  $\delta \mu$  as

$$\begin{pmatrix} \delta \hat{P} \\ \delta \hat{\mu} \end{pmatrix} = \frac{1}{\mu_* \psi_*} \Gamma \begin{pmatrix} \delta P \\ \delta \mu \end{pmatrix}, \quad (50)$$

where  $\Gamma$  is a  $2 \times 2$  diagonal matrix with  $\Gamma_{11} = 1$  and  $\Gamma_{22} = \psi_*$ .

On length scales smaller than the correlation length, correlated clusters of the order parameter formed by critical fluctuations are randomly convected. On larger length scales, where the convection is averaged out,  $\Lambda$  is enhanced by the convection on smaller length scales, and  $\eta_s$  is also enhanced by the nonlinear coupling with the order parameter. In the mixture with  $\psi = 0$ , the viscosity is found to show a weak singularity and its background part is significant[40, 53, 54, 56] unless the mixture is very close to the critical point, unlike  $\Lambda$ . Using curve-fits to experimental data for various temperatures and homogeneous compositions, as shown in Appendix E, we obtain  $\eta_s$  as a function of  $\tau$  and  $\psi$ , and use this function even when  $\psi$  is inhomogeneous. We introduce a dimensionless viscosity  $\hat{\eta}(\hat{r}) \equiv \eta_0(r_{\text{tube}} \hat{r}) / \eta_*$ , where  $\eta_*$  is defined as the value of the singular part of the viscosity for  $\psi = 0$  and  $\tau = \tau_*$  at the equilibrium. A characteristic flow rate is defined as

$$\mathcal{I}_* = \frac{\pi r_{\text{tube}}^4 \mu_* \psi_*}{8 \eta_* L_{\text{tube}}}, \quad (51)$$

which is the flow rate of Hagen-Poiseuille flow of a fluid with the viscosity  $\eta_*$  driven by the pressure gradient  $\mu_* \psi_* / L_{\text{tube}}$ . We non-dimensionalize  $\mathcal{I}$  and  $\mathcal{J}$  to introduce  $\hat{\mathcal{I}}$  and  $\hat{\mathcal{J}}$  as

$$\begin{pmatrix} \hat{\mathcal{I}} \\ \hat{\mathcal{J}} \end{pmatrix} = \frac{1}{\mathcal{I}_*} \Gamma^{-1} \begin{pmatrix} \mathcal{I} \\ \mathcal{J} \end{pmatrix}. \quad (52)$$

$$\begin{array}{ccc}
\begin{pmatrix} -\delta P/T \\ -(\delta\mu)_P/T \end{pmatrix} & \xrightarrow{\mathcal{K}} & \begin{pmatrix} I \\ J \end{pmatrix} \\
N \uparrow & & \downarrow N^T \\
\begin{pmatrix} -\delta P/T \\ -\delta\mu/T \end{pmatrix} & \xrightarrow{\mathcal{L}} & \begin{pmatrix} \mathcal{I} \\ \mathcal{J} \end{pmatrix} \\
\Gamma T/(\mu_*\nu_*) \downarrow & & \uparrow I_*\Gamma \\
\begin{pmatrix} -\delta\hat{P} \\ -\delta\hat{\mu} \end{pmatrix} & \xrightarrow{\hat{\mathcal{L}}} & \begin{pmatrix} \hat{\mathcal{I}} \\ \hat{\mathcal{J}} \end{pmatrix}
\end{array}$$

FIG. 2: Relations given by Eqs. (7), (30), (31), (50), and (52) are shown.

The thermodynamic fluxes conjugate to  $-(\delta\hat{P}/T, \delta\hat{\mu}/T)$  are not  $(\hat{\mathcal{I}}, \hat{\mathcal{J}})$  but  $\mu_*\psi_*\Gamma^{-1}(\mathcal{I}, \mathcal{J})$  with dimensions.

As for  $\Lambda$ , we cannot find out experimental data for  $\psi \neq 0$ . We can extend the previous theoretical result for  $\psi = 0$  to obtain  $\Lambda$  for a homogeneous nonzero value of  $\psi$ , and apply this extended result to a mixture with inhomogeneous composition, as mentioned in Appendix E. Writing  $\Lambda_*$  for the value of  $\Lambda$  for  $\psi = 0$  and  $\tau = \tau_*$ , we define a dimensionless coefficient  $\hat{\Lambda}(\hat{r})$  as  $\Lambda_0(r_{\text{tube}}\hat{r})/\Lambda_*$ . Writing  $z_\psi$  for the dynamic critical exponent for the order-parameter fluctuation, we obtain

$$\hat{\Lambda}(\hat{r}) = \hat{\omega}^{\nu(z_\psi-2)} \left[ \hat{f}''(\hat{\psi}^{(0)}(\hat{r})) \right]^{-1} \quad (53)$$

with the aid of  $\hat{f}''(0) = 1$  at  $\tau = \tau_*$ . Here,  $1/\hat{f}''$  is proportional to the osmotic susceptibility in a mixture with the homogeneous composition. The susceptibility becomes proportional to  $\tau^{-\gamma}$  as  $\tau$  decreases with  $\psi = 0$ , and thus  $\hat{\Lambda}$  is then enhanced with almost the same power as  $\xi$  with respect to  $\tau$ . We here use  $z_\psi = 3.067$ , as mentioned in Appendix E. The same procedure for evaluation of  $\hat{\Lambda}$  as described above is used in Sec. 4.2 of Ref. [16], where  $z_\psi$  is put equal to three.

Substituting Eqs. (28) and (29) into Eqs. (33) and (34), we can calculate a  $2 \times 2$  matrix  $\hat{\mathcal{L}}$ , which is defined so that

$$\begin{pmatrix} \hat{\mathcal{I}} \\ \hat{\mathcal{J}} \end{pmatrix} = -\hat{\mathcal{L}} \begin{pmatrix} \delta\hat{P} \\ \delta\hat{\mu} \end{pmatrix} \quad (54)$$

holds. The components of  $\hat{\mathcal{L}}$  are not the Onsager coefficients because the column vectors on

both the sides above are not conjugate fluxes and forces. From Fig. 2, we find

$$\mathcal{L}_{11} = \frac{T\mathcal{I}_*}{\mu_*\psi_*}\hat{\mathcal{L}}_{11} , \quad \mathcal{L}_{12} = \frac{T\mathcal{I}_*}{\mu_*}\hat{\mathcal{L}}_{12} , \quad \text{and} \quad \mathcal{L}_{22} = \frac{T\mathcal{I}_*\psi_*}{\mu_*}\hat{\mathcal{L}}_{22} , \quad (55)$$

where the second holds if the subscript  $_{12}$  is changed to  $_{21}$  on both sides. We define a functional  $\Omega$  as

$$\Omega[g] = 16 \int_0^1 dq_1 q_1 \hat{\psi}^{(0)}(q_1) \int_{q_1}^1 dq_2 \frac{1}{q_2 \hat{\eta}(q_2)} \int_0^{q_2} dq_3 q_3 g(q_3) , \quad (56)$$

and define another functional  $\Omega_0$  as the right-hand side above with  $\hat{\psi}^{(0)}(q_1)$  being deleted.

Because we have  $\rho^{(0)} = \rho^{(\text{eq})}$ , as mentioned below Eq. (37), we obtain

$$\begin{aligned} \hat{\mathcal{L}}_{11} &= \Omega_0[1] , & \hat{\mathcal{L}}_{12} &= \Omega_0[\hat{\psi}^{(0)}] , & \hat{\mathcal{L}}_{21} &= \Omega[1] , \\ \text{and} \quad \hat{\mathcal{L}}_{22} &= \Omega[\hat{\psi}^{(0)}] + \frac{16\pi}{9} \int_0^1 d\hat{r} \hat{r} \hat{\Lambda}(\hat{r}) . \end{aligned} \quad (57)$$

The coefficient of the last integral is calculated as above in Appendix E. Thanks to this, we need not know the value of  $\Lambda^*$  in later calculations with dimensions. The terms  $\mathcal{L}_{22v}$  and  $\mathcal{L}_{22d}$  are non-dimensionalized to give the first and second terms on the right-hand side of the last entry in Eq. (57), which are denoted by  $\hat{\mathcal{L}}_{22v}$  and  $\hat{\mathcal{L}}_{22d}$ , respectively. Only the latter term depends on  $\hat{\Lambda}$  and is involved in the interdiffusion among all the terms on the right-hand side of Eq. (57), while the other terms depend on  $\hat{\eta}$  and are involved in the convection. Interchanging the orders of the integrations, we have

$$\hat{\mathcal{L}}_{11} = 4 \int_0^1 dq \frac{q^3}{\hat{\eta}(q)} \quad \text{and} \quad \hat{\mathcal{L}}_{12} = \hat{\mathcal{L}}_{21} = 8 \int_0^1 dq_1 q_1 \hat{\psi}^{(0)}(q_1) \int_{q_1}^1 dq_2 \frac{q_2}{\hat{\eta}(q_2)} . \quad (58)$$

As can be seen from Fig. 2, we have

$$\mathcal{K} = \frac{T\mathcal{I}_*}{\mu_*\psi_*} (\Gamma N^{-1})^T \hat{\mathcal{L}} (\Gamma N^{-1}) \quad (59)$$

because  $\Gamma$  is diagonal. Thus, the second entry of Eq. (58) means Onsager's reciprocal relations not only for  $\mathcal{L}$  but also for  $\mathcal{K}$ . Dependence of  $\hat{\mathcal{L}}_{11}$  on  $\hat{\psi}^{(0)}$  is only via  $\hat{\eta}$ , and that of  $\hat{\mathcal{L}}_{22d}$  is only via  $\hat{\Lambda}$ . In contrast with these implicit dependences,  $\hat{\mathcal{L}}_{12} = \hat{\mathcal{L}}_{21}$  and  $\hat{\mathcal{L}}_{22v}$  depend on  $\hat{\psi}^{(0)}$  explicitly. They vanish if  $\hat{\psi}^{(0)}$  vanishes, as mentioned in Sect. III B. These explicit dependences can originate from the difference in the parentheses in Eq. (34), and from the same difference in Eq. (28). The integrand for  $\hat{\mathcal{L}}_{12} = \hat{\mathcal{L}}_{21}$  contains  $\hat{\psi}^{(0)}$  once because of either of the two origins, while the one for  $\hat{\mathcal{L}}_{22v}$  twice because of both the origins. This suggests that  $\hat{\mathcal{L}}_{22v}$  has stronger dependence on  $\hat{\psi}^{(0)}$ .

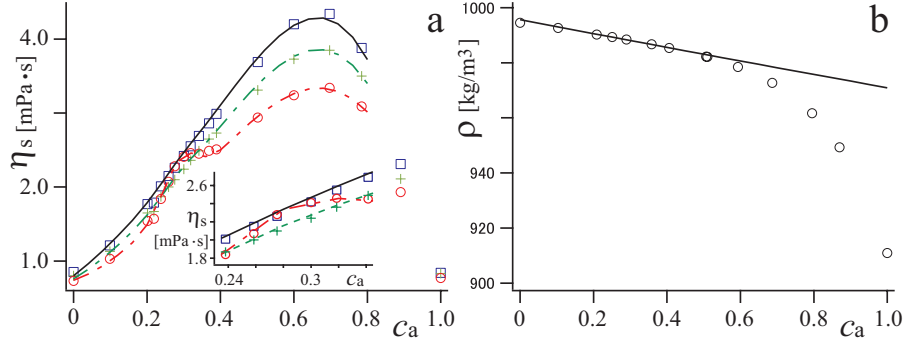


FIG. 3: Experimental data for a mixture of LW;  $c_a$  denotes the mass fraction of 2,6-lutidine. (a) Data of viscosity at  $\tau = 2.25 \times 10^{-2}$ ,  $1.27 \times 10^{-2}$  and  $7.82 \times 10^{-5}$  in Ref. [37] are replotted with black squares, black crosses, and black circles, respectively. Curve fittings for  $c_a < 0.8$  yield the black solid, black dashed, and black dash-dot curves for the respective values of  $\tau$ . A magnified view around the critical composition is shown in the inset. (b) Circles represent experimental data in Table III of Ref. [39] for the relationship between  $\rho$  and  $c_a$  at 306.65 K. The solid curve is obtained by the curve-fit of Eq. (E6) to the data in the region of  $0.2 < c_a < 0.41$ , which contains  $c_{ac}$ .

## V. NUMERICAL RESULTS

The following results are calculated by using the formulae in Sect. IV unless otherwise stated, with the aid of the software Mathematica (Wolfram Research). The mixture in the central region at the equilibrium is assumed to have the critical composition, as mentioned in the preface of Sect. IV. The tube radius is put equal to  $r_{\text{tube}} = 10^{-7}$  m. As discussed in Sect. 6 of Ref. [16], the magnitude of the surface field would not be larger than  $10^{-5}$  m<sup>3</sup>/s<sup>2</sup>, judging from the range of the interaction energy of the hydrogen bond.

### A. Mixture of 2,6-lutidine and water

We first consider a mixture of LW in the homogeneous phase near the lower critical consolute point, taking the former to be the component a. The value of  $\xi_0 = 1.98 \times 10^{-10}$  m in Ref. [36] gives  $\tau_* = 5.12 \times 10^{-5}$ ; we use  $T_c = 307$  K and  $c_{ac} = 0.290$ . The estimate of  $C_2$  in Appendix D gives  $\psi_* = 4.70 \times 10$  kg/m<sup>3</sup>, which leads to  $\mu_* = 1.37 \times 10^{-2}$  m<sup>2</sup>/s<sup>2</sup> at  $T = T_c$ . In Appendix E, we obtain  $\eta_* = 2.44 \times 10^{-3}$  Pa·s and  $\eta_s$  for off-critical compositions

from the experimental data of Refs. [37, 38], part of which are replotted in Fig. 3(a). In this figure, the results at  $\tau = 7.82 \times 10^{-5}$  clearly have a small peak due to the singular part, and its top is located at the value of  $c_a$  slightly larger than  $c_{ac}$  owing to the background part. Assuming the partial volumes to be constants, we find that  $1/\rho$  is a linear function of  $c_a$  from Eq. (3) because of  $\varphi = \rho(2c_a - 1)$ . In the homogeneous phase near the critical temperature, how  $\rho$  depends on  $c_a$  is measurably in Ref. [39]. The curve-fits to the data in Fig. 3(b) gives  $\bar{v}_a = 1.03 \times 10^{-3} \text{ m}^3/\text{kg}$  and  $\bar{v}_b = 1.00 \times 10^{-3} \text{ m}^3/\text{kg}$ , which are respectively regarded as  $\bar{v}_a^{(\text{eq})}$  and  $\bar{v}_b^{(\text{eq})}$ . They are very close to each other in this mixture. From these values, we find  $\rho_c$  and  $\varphi_c$  to be  $9.88 \times 10^2$  and  $-4.15 \times 10^2 \text{ kg/m}^3$ , respectively. In the following calculations, except the ones in Sect. V A 2, the magnitude of  $c_a - c_{ac}$  in the tube at the equilibrium is smaller than 0.15.

### 1. Cases of $h > 0$

Figures 4 - 6 are obtained for  $h = 10^{-7} \text{ m}^3/\text{s}^2$ . This positive value means that the component a (2,6-lutidine) is adsorbed by the tube wall. In Fig. 4(a),  $\hat{\psi}^{(0)}$  is thus positive in the tube and increases towards the wall. As  $\tau$  decreases,  $\hat{\psi}^{(0)}$  increases everywhere in the tube. This increase can be interpreted as that of the thickness of the adsorption layer. It is concomitant with that of  $\xi$  at the tube center, as shown in the inset. At the immediate vicinity of the wall,  $\xi$  decreases with  $\tau$  although rather insensitive to  $\tau$ , and thus the mixture is not close to the critical point even for small  $\tau$ . We calculate  $v_z^{(1)}$  by setting  $\delta\hat{P} = -\varepsilon$  and  $\delta\hat{\mu} = 0$ , and plot the results multiplied by  $\pi r_{\text{tube}}^2/(8\mathcal{I}_*)$  with solid, dashed, and dash-dot curves in Fig. 4(b). The dimensionless product is denoted by  $\hat{v}_z^{(1)}$ . The position of a curve is lowblack with decreasing  $\tau$ , but is not so much deviated from that of the dotted curve, which is obtained for comparison by putting  $\hat{\eta}$  to unity and represents the Hagen-Poiseuille flow. Setting  $\delta\hat{P}$  as above and  $\delta\hat{\mu}$  equal to not zero but  $-\hat{\mathcal{L}}_{11}\delta\hat{P}/\hat{\mathcal{L}}_{12} = \varepsilon\hat{\mathcal{L}}_{11}/\hat{\mathcal{L}}_{12}$  to make  $\hat{\mathcal{I}}$  vanish at  $\tau = 1.25 \times 10^{-5}$ , we calculate  $\hat{v}_z^{(1)}$  and plot the result with the dash-dot-dot curve in Fig. 4(b). The value shown by the curve is positive near the tube center. In a region near the tube wall, the flow driven by  $\delta\hat{\mu}$  surpasses the flow driven by  $\delta\hat{P}$  to make  $\hat{v}_z^{(1)}$  negative. This kind of bidirectional flow is also pointed out in Ref. [24].

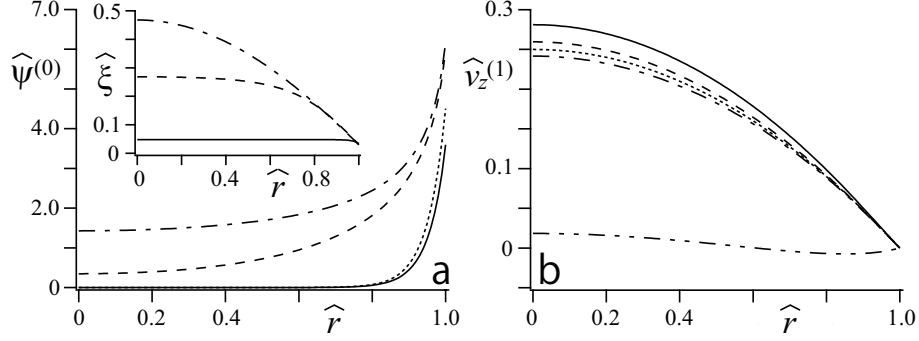


FIG. 4: Results for a mixture of LW are plotted against  $\hat{r}$ . The solid, dashed, dash-dot curves are obtained for  $\tau = 6.4 \times 10^{-3}$ ,  $4.0 \times 10^{-4}$ , and  $1.25 \times 10^{-5}$ , respectively. (a) The equilibrium profile  $\hat{\psi}^{(0)}$  is plotted, while the dimensionless correlation length,  $\hat{\xi} \equiv \xi/r_{\text{tube}}$ , is plotted in the inset. The dotted curve outside the inset represents  $\hat{\psi}^{(0)}$  calculated at  $\tau = 6.4 \times 10^3$  in terms of the Gaussian model. (b) The dimensionless velocity component,  $\hat{v}_z^{(1)}$ , generated by  $\delta\hat{P} = -\varepsilon$  and  $\delta\hat{\mu} = 0$  is plotted. The dotted curve represents  $(1 - \hat{r}^2)/4$ , while the dash-dot-dot curve is obtained by setting  $\delta\hat{\mu}$  so that  $\hat{\mathcal{I}}$  vanishes at  $\tau = 1.25 \times 10^{-5}$ .

At  $\tau = 1.25 \times 10^{-5}$ , the value of  $\xi$  in the immediate vicinity of the wall, 2.98 nm, is still much larger than the molecular length, as required by our model. As  $\tau$  decreases,  $\xi/r_{\text{tube}}$  increases near the tube center, and reaches 0.468 at  $\hat{r} = 0$  and  $\tau = 1.25 \times 10^{-5}$ . There,  $\partial_r v_z$  vanishes and a typical length of the flow is considered to be sufficiently large. In the Hagen-Poiseuille flow,  $\partial_{\hat{r}} \hat{v}_z^{(1)}$  divided by the maximum value of  $\hat{v}_z^{(1)}$  is  $1/(2\hat{r})$ , which is sufficiently larger than  $\hat{\xi}$  for any  $\hat{r}$  shown in the inset of Fig. 4(a). Thus, although there are different ways of defining the typical length, we expect that the flow can be well described in terms of our formulation. As mentioned below Eq. (C4), not a value of  $\xi$  at a point but the values in the tube as a whole should determine the resolution of the coarse-grained hydrodynamics.

The components of  $\hat{\mathcal{L}}$  are calculated by means of Eqs. (57) and (58). In Fig. 5(a),  $\hat{\mathcal{L}}_{11}$  decreases slightly as  $\tau$  decreases, and remains almost the same even if  $\hat{\eta}(\hat{r})$  is replaced by the value for the critical composition irrespective of  $\hat{r}$ . The components  $\hat{\mathcal{L}}_{12}$  and  $\hat{\mathcal{L}}_{22}$  increase eminently as  $\tau$  decreases in Fig. 5(a), while  $\hat{\mathcal{L}}_{12}$  and  $\hat{\mathcal{L}}_{22v} = \hat{\mathcal{L}}_{22} - \hat{\mathcal{L}}_{22d}$  are close to zero at  $\tau = 6.4 \times 10^{-3}$  in Fig. 5(b). The increase of  $\hat{\mathcal{L}}_{22v}$  with decreasing  $\tau$  is larger than that of  $\hat{\mathcal{L}}_{12}$ . Considering the statements in the last paragraph of Sect. IV B, these findings are consistent with the results in Fig. 4(a). In this figure, except for  $\hat{r} \approx 1$ ,  $\hat{\psi}^{(0)}$ , being

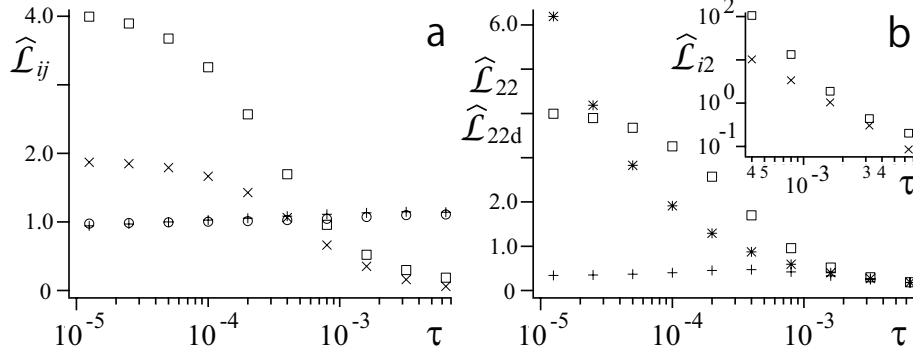


FIG. 5: Semi-logarithmic plots of the components of  $\hat{\mathcal{L}}$  against  $\tau$  for a mixture of LW. (a) The symbols  $\circ$ ,  $\times$ , and  $\square$  represent  $\hat{\mathcal{L}}_{11}$ ,  $\hat{\mathcal{L}}_{12}$ , and  $\hat{\mathcal{L}}_{22}$ , respectively. The symbol  $+$  represents  $\hat{\mathcal{L}}_{11}$  obtained with  $\hat{\eta}$  being put equal to the value for the critical composition homogeneously. (b) The symbol  $\square$  represents  $\hat{\mathcal{L}}_{22}$ , and is the replot of the same symbol in (a); the symbol  $+$  represents  $\hat{\mathcal{L}}_{22d}$ . The symbol  $*$  represents  $\hat{\mathcal{L}}_{22d}$  obtained with  $\hat{\Lambda}$  being put equal to the value for the critical composition homogeneously. The inset shows logarithmic plots of  $\hat{\mathcal{L}}_{12}$  ( $\times$ ) and  $\hat{\mathcal{L}}_{22}$  ( $\square$ ) calculated on the basis of the Gaussian model.

approximately zero at  $\tau = 6.4 \times 10^{-3}$ , increases distinctly as  $\tau$  decreases. The increase of  $\hat{\mathcal{L}}_{22}$  with decreasing  $\tau$  is mainly caused by that of  $\mathcal{L}_{22v}$  because the change of  $\hat{\mathcal{L}}_{22d}$  is slight in Fig. 5(b). Assuming  $\hat{\Lambda}$  to be homogeneously equal to the value for the critical composition, we calculate  $\hat{\mathcal{L}}_{22d}$  and plot the results with the symbol  $*$  for comparison in Fig. 5(b). The results increase as  $\tau$  decreases, which represents the critical enhancement of  $\Lambda$ .

In the tube,  $\hat{\psi}^{(0)}(\hat{r})$  increases as  $\tau$  decreases. The increase of  $\hat{\psi}^{(0)}$  tends to make the mixture farther from the critical point, while the decrease of  $\tau$  has the opposite tendencies. This would cause the non-monotonic change of  $\hat{f}''$  at  $r = 0$  shown in Fig. 6(a), although the inset shows that the change of  $\hat{\xi}$  at  $r = 0$  is monotonic. They are both involved in Eq. (53) because of Eq. (42). Accordingly,  $\hat{\Lambda}$  near  $r = 0$  is largest at the intermediate value of  $\tau$  in Fig. 6(b). This causes non-monotonic change of  $\hat{\mathcal{L}}_{22d}$  represented by the symbol  $+$  in Fig. 5(b). Thus, we should take into account the inhomogeneity of  $\hat{\psi}^{(0)}$  appropriately in calculating  $\hat{\mathcal{L}}_{22d}$  not to overestimate the critical enhancement of  $\Lambda$ .

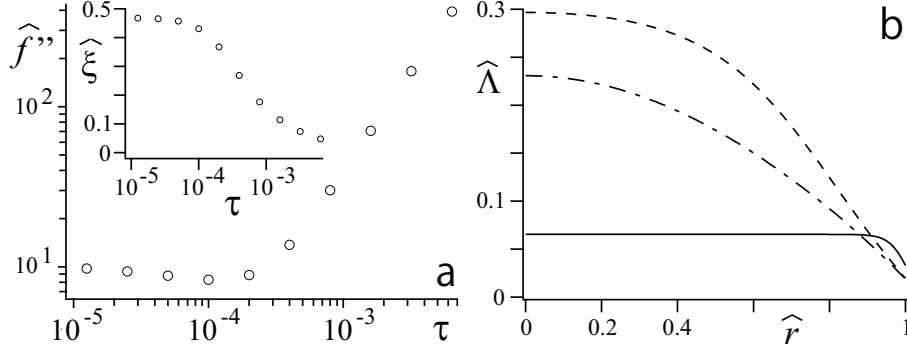


FIG. 6: Results for a mixture of LW. (a) A logarithmic plot of  $\hat{f}''(\hat{\psi}^{(0)}(0))$  against  $\tau$  is shown. The inset shows a semilogarithmic plot of  $\hat{\xi}$  at  $\hat{r} = 0$  against  $\tau$ . (b) Values of  $\hat{\Lambda}$  are plotted against  $\hat{r}$ . The solid, dashed, dash-dot curves represent the results for  $\tau = 6.4 \times 10^{-3}$ ,  $4.0 \times 10^{-4}$ , and  $1.25 \times 10^{-5}$ , respectively.

### 2. Results based on the Gaussian model

For comparison, we show some results calculated on the basis of the Gaussian model, where Eq. (44) is approximated to be a quadratic function of  $\hat{\psi}$  with  $\hat{\omega}$ , and thus  $\hat{\xi}$ , being assumed to be homogeneous. This approximation can work well if  $\tau$  is not so small and if  $\psi$  is close to zero, as mentioned in Appendix F. At  $\tau = 6.4 \times 10^{-3}$ , the values of  $\hat{\psi}^{(0)}$  shown by the dotted and solid curves in Fig. 4(a) are not so much different. However, the values of  $\hat{\psi}^{(0)}$  in the Gaussian model range from 3.5 to 29 at  $\tau = 4.0 \times 10^{-4}$ , and are much larger than the values shown by the dashed curve in Fig. 4(a). Accordingly, the values of  $\hat{\mathcal{L}}_{12}$  and  $\hat{\mathcal{L}}_{22}$  in the inset of Fig. 5(b) are only slightly larger than the ones in Fig. 5(a) at  $\tau = 6.4 \times 10^{-3}$ , respectively, but the former values become much larger than the latter values, respectively, as  $\tau$  becomes smaller.

### 3. Effects caused by changing the sign of $h$

The background part of  $\eta_s$  at a value of  $\tau$  increases with  $c_a$  around  $c_{ac}$  in Fig. 3(a). From Fig. 4(a),  $\hat{\psi}^{(0)}$ , and thus  $c_a - c_{ac}$ , are found to be positive, and increases monotonically towards the tube wall. However, owing to the singular part,  $\eta_s$  does not change monotonically with  $\hat{r}$  in Fig. 7(a). Its increase with decreasing  $\tau$  is consistent with the monotonic



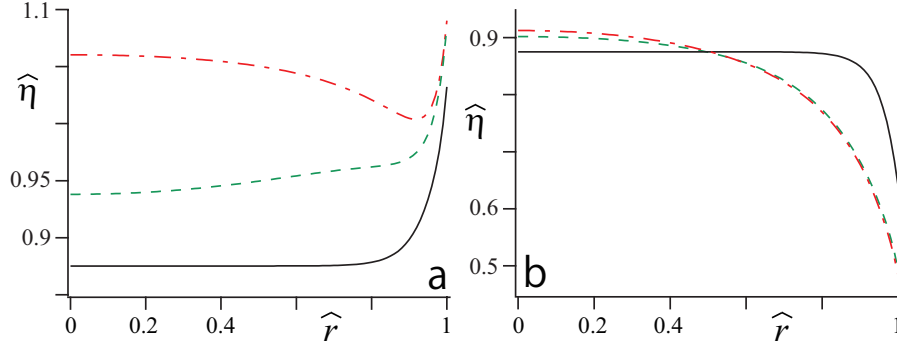


FIG. 7: Values of  $\hat{\eta}$  for a mixture of LW are calculated and plotted against  $\hat{r}$ . The black solid, black dashed, black dash-dot curves represent the results for  $\tau = 6.4 \times 10^{-3}$ ,  $4.0 \times 10^{-4}$ , and  $1.25 \times 10^{-5}$ , respectively. At these values of  $\tau$ ,  $\hat{\eta}$  takes 0.875, 0.922 and 1.06 for the critical composition, respectively. (a) We use  $h = 1.0 \times 10^{-7} \text{ m}^3/\text{s}^2$  in (a), while  $h = -1.0 \times 10^{-7} \text{ m}^3/\text{s}^2$  in (b).

decrease of  $\hat{v}_z^{(1)}$  with  $\tau$  in Fig. 4(b) and that of  $\hat{\mathcal{L}}_{11}$  in Fig. 5(a). When we change the sign of  $h$  to set  $h = -1.0 \times 10^{-7} \text{ m}^3/\text{s}^2$ , the sign of  $\hat{\psi}^{(0)}$  is also changed with its magnitude unchanged, and  $c_a$  is smaller than  $c_{ac}$  in the tube. Then, as shown in Fig. 7(b),  $\hat{\eta}$  at a value of  $\tau$  monotonically decreases towards the tube wall. The extent of the decrease at  $\tau = 6.4 \times 10^{-3}$ , being the smallest in Fig. 7(b), is still larger than the range of the values at a value of  $\tau$  in Fig. 7(a). The curves for the same value of  $\tau$  in these figures are different from each other because the background part as a function of  $c_a$  is asymmetric with respect to  $c_{ac}$ . In Fig. 7(b), as  $\tau$  decreases from  $6.4 \times 10^{-3}$  to  $4.0 \times 10^{-4}$ ,  $\hat{\eta}$  decreases distinctly near the tube wall, which comes from the decrease of the background part with  $\tau$  shown in Fig. 3(a). Accordingly, then  $\hat{\mathcal{L}}_{11}$  increases in Fig. 8. As  $\tau$  decreases further,  $\hat{\eta}$  and  $\hat{\mathcal{L}}_{11}$  become rather insensitive to  $\tau$ . In Fig. 5(a), the values of circle ( $\circ$ ) and cross ( $+$ ) happen to coincide approximately. The latter values decreases with  $\tau$  in a range of small  $\tau$  because of the critical enhancement of  $\eta_s$ , and exhibit a less distinct change than the values of asterisk in Fig. 5(b) because of a weaker singularity. The coincidence does not occur in Fig. 8, where the  $c_a$  in the tube changes on the left-hand side of  $c_{ac}$  in Fig. 3(a). Thus, with the inhomogeneity of  $\psi$  considered properly,  $\hat{\mathcal{L}}_{11}$  largely depends on the non-universal background part of  $\eta_s$ .

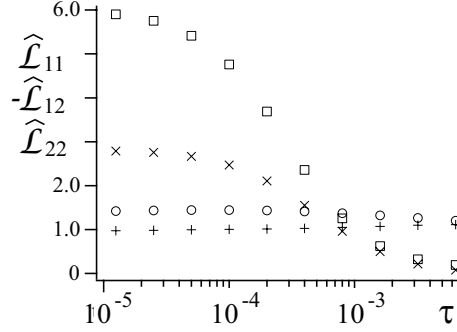


FIG. 8: Plots of  $\hat{\mathcal{L}}_{11}$  ( $\circ$ ),  $-\hat{\mathcal{L}}_{12}$  ( $\times$ ), and  $\hat{\mathcal{L}}_{22}$  ( $\square$ ) against  $\tau$ . We use  $h = -10^{-7} \text{ m}^3/\text{s}^2$ , which is negative of the value used in Figs. 5 and 6. For comparison, the same data as shown by the circles in Fig. 5(a) are here replotted with crosses ( $+$ ).

For  $h < 0$ , the value of  $\hat{\mathcal{L}}_{12}$  becomes negative because of  $\hat{\psi}^{(0)} < 0$  in the second entry of Eq. (58). The value of  $\hat{\mathcal{L}}_{22d}$  is irrespective of the sign of  $h$  because of Eq. (53). The magnitudes of these values increase with decreasing  $\tau$  because  $\hat{\psi}^{(0)}$  negatively increases. Suppose  $\delta P = 0$  and  $\delta c_a < 0$ , which gives  $(\delta\mu)_P = \delta\mu < 0$ . Then,  $\hat{\mathcal{L}}_{12} < 0$  yields  $\mathcal{I} < 0$ , which means that the total mass flow goes into the left reservoir, considering Eqs. (33), (35), and (55). This flow tends to relax the mass-fraction difference between the reservoirs because the component a is depleted in the tube for the value of  $h$  considered here. In a range of small  $\tau$ , we find that each component of  $\hat{\mathcal{L}}$  exhibits a larger change for  $h < 0$  than for  $h > 0$  by comparing Fig. 5(a) with Fig. 8. This comes from the difference in the dependences of  $\hat{\eta}$  on  $\tau$  and  $\hat{r}$  between the graphs of Fig. 7, and thus from the asymmetry of the background part of  $\eta_s$ .

#### 4. Mass flow rates of the components

We set  $L_{\text{tube}} = 10^{-6} \text{ m}$ , which is much larger than  $r_{\text{tube}} = 10^{-7} \text{ m}$ , and have  $\mathcal{I}_* = 1.04 \times 10^{-20} \text{ m}^3/\text{s}$  at  $T = T_c$ . We define  $c_{\text{aR}}^{(\text{flux})}$  as  $d\mathcal{M}_{\text{aR}}/(dt)$  divided by the total mass flow rate. This quantity can be interpreted as the mass fraction of the component a in the mixture flowing into the right reservoir per unit time if the mass flow rates share the same sign. Otherwise,  $c_{\text{aR}}^{(\text{flux})}$  becomes negative, can have the magnitude larger than unity, and loses the meaning of a mass fraction.

We first set  $\delta P = -10^4 \text{ kg}/(\text{m} \cdot \text{s}^2) \approx -0.1 \text{ atm}$  and  $(\delta\mu)_P \propto \delta c_a = 0$  to consider flows driven by pressure difference. The Reynolds number approximately equals  $4 \times 10^{-4}$ , which is much smaller than unity and validates the assumption of the laminar flow. Substituting Eq. (35) into Eq. (36), we use Eqs. (4) and (55) to find that  $d\mathcal{M}_{nR}/(dt)$  is given by  $\delta P$  multiplied by

$$-\frac{\mathcal{I}_* \rho_n^{(\text{eq})}}{\mu_* \psi_*} \left( \hat{\mathcal{L}}_{11} + \psi_* \bar{v}_-^{(\text{eq})} \hat{\mathcal{L}}_{12} \right) \mp \frac{\mathcal{I}_*}{2\mu_*} \left( \hat{\mathcal{L}}_{12} + \psi_* \bar{v}_-^{(\text{eq})} \hat{\mathcal{L}}_{22} \right), \quad (60)$$

where the double sign implies the same as in Eq. (36). The mass flow rates for  $h = 10^{-7} \text{ m}^3/\text{s}^2$  are thus calculated and are plotted in Fig. 9(a). For the values of the open circle and square,  $c_{\text{aR}}^{(\text{flux})}$  increases slightly as  $\tau$  decreases. The values are larger than  $c_{\text{ac}}$ ; its value is 0.291 for  $\tau = 6.4 \times 10^{-3}$  and 0.336 for  $\tau = 1.25 \times 10^{-5}$ . Because of  $\psi_* \bar{v}_-^{(\text{eq})} = 6.00 \times 10^{-4}$ , the second terms in the two sets parentheses in Eq. (60) are negligible for the values of  $\hat{\mathcal{L}}_{ij}$  shown in Fig. 5(a), where  $\hat{\mathcal{L}}_{12}$  is larger than approximately one thirds of  $\hat{\mathcal{L}}_{22}$ . Hence, Eq. (60) can be approximated to be

$$-\frac{\mathcal{I}_* \rho_n^{(\text{eq})}}{\mu_* \psi_*} \hat{\mathcal{L}}_{11} \mp \frac{\mathcal{I}_*}{2\mu_*} \hat{\mathcal{L}}_{12}. \quad (61)$$

The first term of Eq. (61) mainly contributes to the values of the open circle and square, and the change of  $c_{\text{aR}}^{(\text{flux})}$  is mainly caused by the second term representing the cross effect. The change can be also realized intuitively, considering that  $h > 0$  means that the component a is adsorbed in the tube. The decrease of  $d\mathcal{M}_{\text{bR}}/(dt)$  with  $\tau$ , shown by  $\square$  in Fig. 9(a), can be explained by the distinct increase of  $\hat{\eta}$  near the tube center, where the component b is more concentrated, in Fig. 7(a).

In the absence of the preferential adsorption ( $h = 0$ ),  $\hat{\psi}^{(0)} = 0$  gives  $\hat{\mathcal{L}}_{12} = \hat{\mathcal{L}}_{21} = 0$  and  $\hat{\mathcal{L}}_{22\text{v}} = 0$ ; the values of  $+$  in Fig. 5(a) and those of  $*$  in Fig. 5(b) are used as those of  $\hat{\mathcal{L}}_{11}$  and  $\hat{\mathcal{L}}_{22}$ , respectively. Then, setting  $\delta P$  and  $(\delta\mu)_P$  as above, we use Eq. (60) to obtain the values of the solid circle and asterisk in Fig. 9(a). The first term of Eq. (61) mainly contributes to the values of these symbols;  $c_{\text{aR}}^{(\text{flux})}$  remains very close to  $c_{\text{ac}} = 0.290$  and ranges between  $c_{\text{ac}}$  and 0.2901. The values of the symbols decrease with  $\tau$  in a range of small  $\tau$ , which is caused by the critical enhancement of the viscosity. The enhancement is evaded in the presence of the preferential adsorption.

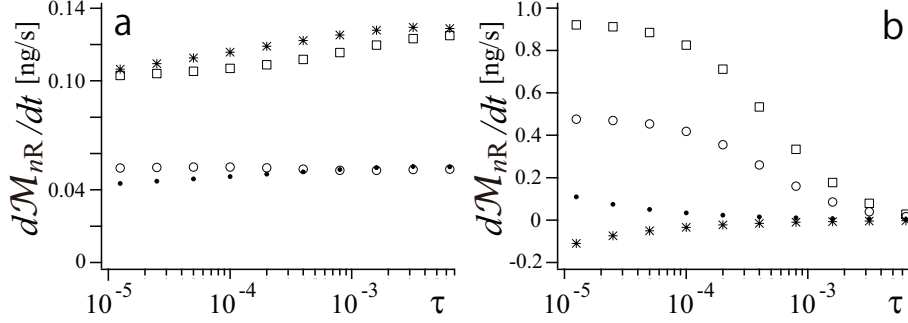


FIG. 9: Plots of  $d\mathcal{M}_{\text{aR}}/(dt)$  (open and solid circles) and  $d\mathcal{M}_{\text{bR}}/(dt)$  (squares and asterisks) against  $\tau$  for a mixture of LW are shown. The values of the open circle and square are obtained for  $h = 1.0 \times 10^{-7} \text{ m}^3/\text{s}^2$ , while those of the solid circle and asterisk for  $h = 0$ . We use  $\delta P = 10^4 \text{ kg}/(\text{m}\cdot\text{s}^2)$  and  $(\delta\mu)_P = 0$  (a), and  $\delta P = 0$  and  $(\delta\mu)_P = -10^3 \text{ m}^2/\text{s}^2$  (b).

Next, we set  $\delta P = 0$  and  $(\delta\mu)_P = \delta\mu = -10^3 \text{ m}^2/\text{s}^2$  to consider flows driven by mass-fraction difference. If the mixture is ideal, the latter value amounts to  $\delta c_a = -1.31 \times 10^{-2}$ , whose magnitude is much smaller than  $c_{\text{ac}}$ . Like Eq. (60), we find  $d\mathcal{M}_{\text{nR}}/(dt)$  to be given by  $(\delta\mu)_P$  multiplied by

$$-\frac{\mathcal{I}_* \rho_n^{(\text{eq})}}{\mu_*} \hat{\mathcal{L}}_{12} \mp \frac{\mathcal{I}_* \psi_*}{2\mu_*} \hat{\mathcal{L}}_{22}, \quad (62)$$

where the double sign means the same as in Eq. (36). The mass flow rates for  $h = 10^{-7} \text{ m}^3/\text{s}^2$  are plotted in Fig. 9(b), where the values of the open circle and square increase distinctly as  $\tau$  decreases. These values are 0.476 and 0.921 ng/s, respectively, at  $\tau = 1.25 \times 10^{-5}$ , where the values of the first term of Eq. (62) for a and b are 0.405 and 0.991 ng/s, respectively. The first term, responsible for the increase of the total mass flow rate, mainly contribute to the mass flow rates, although  $\hat{\mathcal{L}}_{22}$  is larger than  $\hat{\mathcal{L}}_{12}$  in Fig. 5(a). This comes from the difference in the coefficient between the terms of Eq. (62), which goes back to the one between the terms on the right-hand side of Eq. (36). In the absence of the preferential adsorption ( $h = 0$ ),  $\hat{\mathcal{L}}_{12}$  vanishes and the total mass flow rate vanishes, which can be read from solid circles and asterisks in Fig. 9(b). The magnitudes of the values of these symbols increase as  $\tau$  decreases, which represents the critical enhancement of  $\Lambda$ . The enhancement is evaded in the presence of the preferential adsorption. Thus, the near-critical increases of the total mass flow rate driven by mass-fraction difference in the presence of the preferential adsorption are caused not by the critical enhancement of the transport coefficient but by the increase of the convection associated with  $\mathcal{L}_{12}$ . The mass flow rates of the components

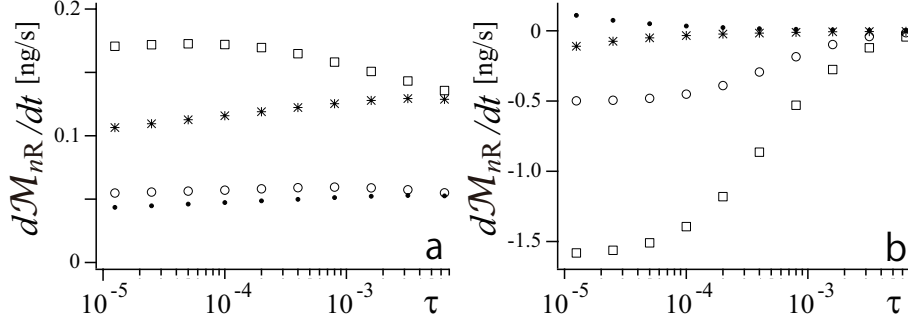


FIG. 10: The same plots of  $dM_{nR}/(dt)$  as in Fig. 9, except that the sign of  $h$  is inverted. The results shown by solid circles and asterisks in (a) and (b) are the same as the ones shown by these symbols in Fig. 9(a) and (b), respectively.

are subsidiarily affected by  $\mathcal{L}_{22v}$ .

For  $h = -10^{-7} \text{ m}^3/\text{s}^2$ , we use Eqs. (60) and (62) to calculate the mass flow rates driven by pressure difference and mass-fraction difference, respectively. The respective results are plotted in Figs. 10(a) and (b), where the same results for  $h = 0$  as shown in Fig. 9 are replotted for comparison. The first term of Eq. (61) mainly contributes to the the results of open circle and square in Fig. 10(a). For them,  $c_{aR}^{(\text{flux})}$  decreases from  $0.289 (< c_{ac})$  to  $0.243$  as  $\tau$  decreases from  $6.4 \times 10^{-3}$  to  $1.25 \times 10^{-5}$ , which is reasonable because  $h < 0$  means that the component a is depleted in the tube. This change is mainly caused by the second term of Eq. (61). The value of the square increases as  $\tau$  decreases in a region of large  $\tau$  in Fig. 10(a), which can be realized by noting that the dashed and dash-dot curves are distinctly below the solid curve near the tube wall, where the component b is more concentrated, in Fig. 7(b). In a flow driven by mass-fraction difference, the mass flow rates, shown by the open circle and square, become negatively larger as  $\tau$  decreases in Fig. 10(b). They are  $-0.499$  and  $-1.58 \text{ ng/s}$ , respectively at  $\tau = 1.25 \times 10^{-5}$ , where the values of the first term of Eq. (62) for a and b are  $-0.604$  and  $-1.48 \text{ ng/s}$ , respectively. The first term mainly contributes to the values of the open circle and square.

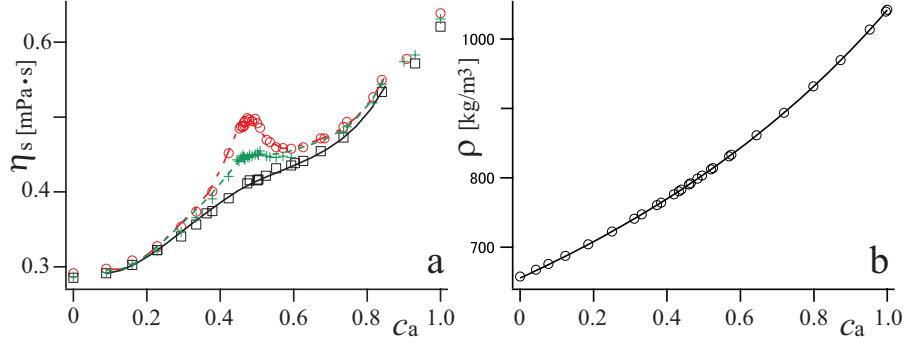


FIG. 11: Experimental data for a mixture of NEMP with various values of  $c_a$  (the mass fraction of nitroethane). (a) Data of viscosity at  $\tau = 1.47 \times 10^{-4}$ ,  $1.82 \times 10^{-3}$ , and  $1.19 \times 10^{-2}$  of Ref. [41] are shifted, as mentioned in Appendix E, to yield the values of black circles, black crosses, and black squares, respectively. Curve fits to the data for  $0.08 < c_a < 0.85$  yield the black dash-dot, black dashed, and black solid curves for the respective values of  $\tau$ . (b) Circles represent experimental data of Ref. [42] for the relationship between  $\rho$  and  $c_a$  at 300.153 K. The solid curve is obtained by the curve-fit of Eq. (E6) to the data for  $0.3 < c_a < 0.6$ .

### B. Mixture of nitroethane and 3-methylepentane

We consider a mixture of NEMP in the homogeneous phase near the upper critical consolute point ( $T_c = 300$  K and  $c_{ac} = 0.466$ ), taking the former component to be the component a. We have  $\xi_0 = 2.30 \times 10^{-10}$  m[40] to obtain  $\tau_* = 6.49 \times 10^{-5}$ . The estimate of  $C_2$  in Appendix D gives  $\psi_* = 4.19 \times 10$  kg/m<sup>3</sup>, which leads  $\mu_* = 1.50 \times 10^{-2}$  m<sup>2</sup>/s<sup>2</sup> at  $T = T_c$ . We use the experimental data of Refs. [40, 41] to calculate  $\eta_* = 5.10 \times 10^{-4}$  Pa·s and  $\eta_s$  for off-critical compositions in Appendix E. As shown in Fig. 11(a), the value of  $\eta_s$  exhibits a less distinct change with  $c_a$  in this mixture than in Fig. 3(a). Its background part of this mixture increases as  $\tau$  decreases, unlike in Fig. 3(a) showing the results near the lower consolute point of a mixture. Using the same procedure as used in Fig. 3(b), we apply curve-fit to the data of Ref. [42] in Fig. 11(b) and obtain  $\bar{v}_a^{(eq)} = 9.60 \times 10^{-4}$  m<sup>3</sup>/kg and  $\bar{v}_b^{(eq)} = 1.53 \times 10^{-3}$  m<sup>3</sup>/kg, which leads to  $\rho_c = 7.92 \times 10^2$  kg/m<sup>3</sup> and  $\varphi_c = -5.46 \times 10$  kg/m<sup>3</sup>. In the following calculations, the magnitude of  $c_a - c_{ac}$  in the tube at the equilibrium is smaller than 0.17.

The components of  $\hat{\mathcal{L}}$  are calculated by means of Eqs. (57) and (58). Figures 12(a) and (b)

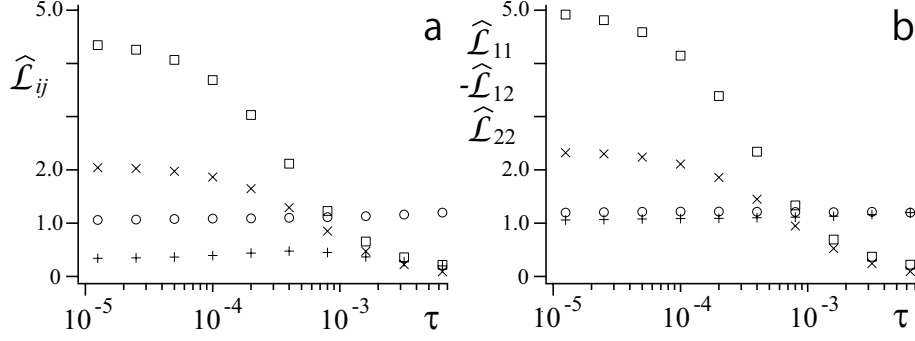


FIG. 12: Semi-logarithmic plots of the components of  $\hat{\mathcal{L}}$  against  $\tau$  for a mixture of NEMP. (a) The symbols  $\circ$ ,  $\times$ ,  $\square$ , and  $+$  represent  $\hat{\mathcal{L}}_{11}$ ,  $\hat{\mathcal{L}}_{12}$ ,  $\hat{\mathcal{L}}_{22}$ , and  $\hat{\mathcal{L}}_{22d}$ , respectively, for  $h = 10^{-7} \text{ m}^3/\text{s}^2$ . (b) The symbols  $\circ$ ,  $\times$ , and  $\square$  represent  $\hat{\mathcal{L}}_{11}$ ,  $-\hat{\mathcal{L}}_{12}$ , and  $\hat{\mathcal{L}}_{22}$ , respectively, for  $h = -10^{-7} \text{ m}^3/\text{s}^2$ . For comparison, the same data as shown by the circles in Fig. 5(a) are here replotted with crosses.

are obtained for  $h = 10^{-7} \text{ m}^3/\text{s}^2$  and for  $h = -10^{-7} \text{ m}^3/\text{s}^2$ , respectively. As  $\tau$  decreases,  $\hat{\mathcal{L}}_{12} = \hat{\mathcal{L}}_{21}$  becomes positively larger for  $h > 0$  and negatively larger for  $h < 0$ . Then,  $\hat{\mathcal{L}}_{22}$  becomes larger, while  $\hat{\mathcal{L}}_{11}$  and  $\hat{\mathcal{L}}_{22d}$  exhibit much less distinct changes. These two terms depend on  $\hat{\psi}^{(0)}$  via the transport coefficients, whose critical enhancement is evaded by the preferential adsorption. These properties are the same as shown in Figs. 5(a) and Fig. 8 for a mixture of LW. Difference between the values of open circle and cross at a value of  $\tau$  in Fig. 12(b) is much smaller than the one in Fig. 8. This is consistent with the small change of  $\eta_s$  with  $c_a$  mentioned above.

We set  $L_{\text{tube}} = 10^{-6} \text{ m}$ , which leads to  $\mathcal{I}_* = 4.84 \times 10^{-20} \text{ m}^3/\text{s}$  at  $T = T_c$ . For  $h = 10^{-7} \text{ m}^3/\text{s}^2$ , the mass flow rates driven by pressure difference are calculated by using Eq. (60) and plotted in Fig. 13(a). The values of the open circle and square in Fig. 13(a) exhibit a weak dependence on  $\tau$ , as in Fig. 9(a) for a mixture of LW. For them,  $c_{\text{aR}}^{(\text{flux})}$  is larger than  $c_{\text{ac}}$ , and slightly increases as  $\tau$  decreases. Its value is 0.467 for  $\tau = 6.4 \times 10^{-3}$  and 0.516 for  $\tau = 1.25 \times 10^{-5}$ . This is expected because the component a is adsorbed in the tube. This mixture has  $\psi_* \bar{v}_-^{(\text{eq})} = -1.18 \times 10^{-2}$ , whose magnitude is larger than the corresponding value in a mixture of LW. Still, Eq. (61) remains here to give a good approximation to Eq. (60). Thus, as in Fig. 9(a), the first term of Eq. (61) mainly contributes to the values of the symbols  $\circ$  and  $\square$  in Fig. 13(a), while the second term mainly contributes to the change of  $c_{\text{aR}}^{(\text{flux})}$ . The values of the open circle and square at a value of  $\tau$  are close to each other and

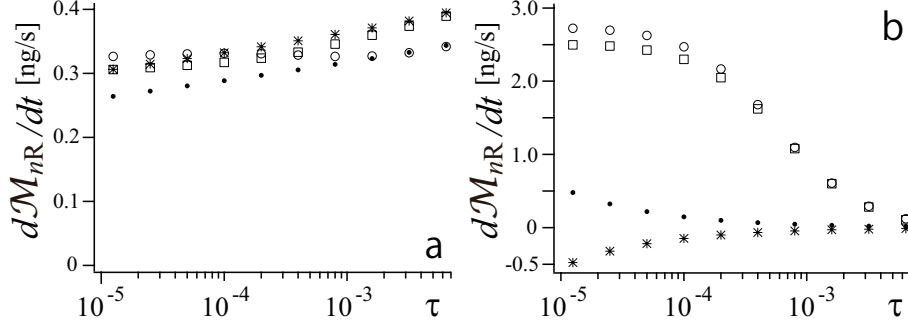


FIG. 13: Plots of  $d\mathcal{M}_{aR}/(dt)$  (open and solid circles) and  $d\mathcal{M}_{bR}/(dt)$  (squares and asterisks) against  $\tau$  for a mixture of NEMP are shown. The values of the open circle and square are obtained for  $h = 1.0 \times 10^{-7} \text{ m}^3/\text{s}^2$ , while those of the solid circle and asterisk for  $h = 0$ . We use  $\delta P = 10^4 \text{ kg}/(\text{m}\cdot\text{s}^2)$  and  $(\delta\mu)_P = 0$  (a), and  $\delta P = 0$  and  $(\delta\mu)_P = -10^3 \text{ m}^2/\text{s}^2$  (b).

larger than the respective ones in Fig. 9(a). These properties appear because this mixture has  $\rho_b^{(\text{eq})}/\rho_a^{(\text{eq})} = 1/c_{ac} - 1$  closer to unity and because it has smaller  $\eta_s$ , respectively. For  $h = 0$ , we obtain the values of the solid circle and asterisk in Fig. 13(a). The first term of Eq. (61) mainly contributes to the values of these symbols;  $c_{aR}^{(\text{flux})}$  remains very close to  $c_{ac} = 0.466$  and ranges between  $c_{ac}$  and 0.463. The values of the symbols decrease with  $\tau$  because of the critical enhancement of  $\eta_s$ .

For  $h = 10^{-7} \text{ m}^3/\text{s}^2$ , the mass flow rates driven by mass-fraction difference are calculated by using Eq. (62) and plotted in Fig. 13(b). The values of the open circle and square in Fig. 13(b) increase eminently as  $\tau$  decreases. Their respective values are 2.72 and 2.50 ng/s at  $\tau = 1.25 \times 10^{-5}$ , where the values of the first term of Eq. (62) for a and b are 2.43 and 2.79 ng/s, respectively. The first term mainly contributes to the results, and is responsible for the total mass flow rate, as in Fig. 9(b). The mass flow rates of the components are subsidiarily affected by the second term. The values of the symbols at a value of  $\tau$  are close to each other, as compared with the ones in Fig. 9(b). This is because  $\rho_a^{(\text{eq})}$  is closer to  $\rho_b^{(\text{eq})}$  in this mixture. The mass flow rates for  $h = 0$  are shown by solid circles and asterisks in Fig. 13(b). As in Fig. 9(b), their sum vanishes because of  $\hat{\mathcal{L}}_{12} = 0$ , and their magnitudes increase as  $\tau$  decreases because of the critical enhancement of  $\Lambda$ .

The mass flow rates driven by pressure difference and mass-fraction difference are calculated



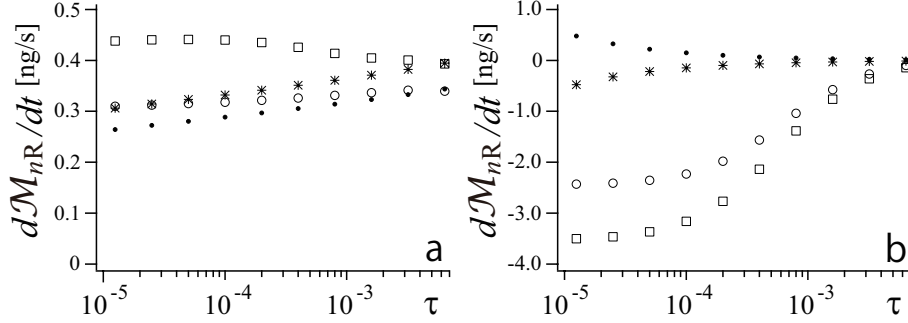


FIG. 14: The same plots of  $d\mathcal{M}_{nR}/(dt)$  as in Fig. 13, except that the sign of  $h$  is inverted. The results shown by solid circles and asterisks in (a) and (b) are the same as the ones shown by these symbols in Fig. 13(a) and (b), respectively.

for  $h = -10^{-7} \text{ m}^3/\text{s}^2$  and are plotted in Figs. 14(a) and (b), respectively, where the same results for  $h = 0$  as shown in Fig. 13 are replotted for comparison. The first term of Eq. (61) mainly contributes to the results of the open circle and square in Fig. 14(a). For them,  $c_{\text{aR}}^{(\text{flux})}$ , being smaller than  $c_{\text{ac}}$ , decreases from 0.463 to 0.414 as  $\tau$  decreases from  $6.4 \times 10^{-3}$  to  $1.25 \times 10^{-5}$ . This change is expected because the component a is depleted in the tube, and is mainly caused by the second term of Eq. (61). The values of the open circle and square in Fig. 14(b) become negatively larger as  $\tau$  decreases. Their respective values are  $-2.43$  and  $-3.50 \text{ ng/s}$  at  $\tau = 1.25 \times 10^{-5}$ , where the values of the first term for a and b are  $-2.76$  and  $-3.17 \text{ ng/s}$ , respectively. The first term in Eq. (62) mainly contributes to the values of the open circle and square in Fig. 14(b). These findings are qualitatively the same as the ones in Fig. 10.

## VI. DISCUSSION

Whether  $\rho^{(0)}$  is homogeneous or not does not depend on the compressibility of the mixture, as mentioned at the end of Sect. II B, because it is the equilibrium density. Even if the surface energy is not a function of  $\rho$  at  $\partial V_{\text{tot}}$ ,  $\rho^{(0)}$  can be inhomogeneous when the free-energy functional is not separated into  $\rho$ - and  $\psi$ -dependent parts. In Sect. III B, not assuming homogeneous  $\rho^{(0)}$ , we derive Eqs. (28) and (29), which are substituted into Eqs. (33) and (34) to yield the expressions of the Onsager coefficients of Eq. (35). Unlike the coefficient  $\mathcal{L}_{11}$  and the term  $\mathcal{L}_{22\text{d}}$ , the coefficient representing the cross effect,  $\mathcal{L}_{12}(= \mathcal{L}_{21})$ ,

and the term  $\mathcal{L}_{22v}$  explicitly depend on  $\varphi^{(0)} - \rho^{(0)}\varphi^{(\text{eq})}/\rho^{(\text{eq})}$ . Among these coefficients and terms,  $\mathcal{L}_{22d}$  is involved in the interdiffusion and depends on the transport coefficient  $\Lambda$ , while the others are involved in the convection and depend on the other transport coefficient  $\eta_s$ . The coefficients  $\mathcal{L}_{12} = \mathcal{L}_{21}$  and the term  $\mathcal{L}_{22v}$  emerges in the presence of the preferential adsorption. In the absence, we have the usual Hagen-Poiseuille flow with the interdiffusion.

A compressible mixture can have nonzero  $\rho^{(1)}$ , which is involved in Eq. (9). The right-hand side of Eq. (12) becomes  $\rho^{(0)}\nabla\mu_+^{(1)} + \varphi^{(0)}\nabla\mu^{(1)}$  up to the order of  $\varepsilon$ . Thus,  $\rho^{(1)}$  affects the dynamics up to this order via  $\mu_+^{(1)}$  and  $\mu^{(1)}$ . In our problem, the left-hand sides of Eq. (26) are determined by a set of the forces  $(-\delta P/T, \delta\mu/T)$ , and thus  $\rho^{(1)}$  need not be explicitly considered in deriving Eq. (27). Hence, the mixture is not required to be incompressible in the present study, unlike in Ref. [16]. The set is determined by  $(\delta P, \delta c_a)$  because of Eq. (4). The difference between the pressures felt by the pistons, *i.e.*,  $\delta P$ , can cause nonzero  $\delta\mu$  and the interdiffusion in the mixture with  $\bar{v}_-^{(\text{eq})} \neq 0$  even if  $\delta c_a$  vanishes.

For a mixture of 2,6-lutidine and water (LW) and for a mixture of nitroethane and 3-methylpentane (NEMP), we numerically calculate the Onsager coefficients in Sect. V by applying the renormalized local functional theory[12] to the formulae obtained in Sect. IV B and by assuming the critical composition in the central region of the reservoir, *i.e.*,  $\varphi_c = \varphi^{(\text{eq})}$ . In this calculation,  $\rho^{(0)}$  becomes homogeneous, and we have  $\rho^{(0)} = \rho^{(\text{eq})} = \rho_c$ . Thus,  $\mathcal{L}_{12} = \mathcal{L}_{21}$  and  $\mathcal{L}_{22v}$  explicitly depend on  $\psi^{(0)} \equiv \varphi^{(0)} - \varphi_c$ , as can be seen from Eqs. (57) and (58). The influences of nonzero  $\bar{v}_-^{(\text{eq})}$  to the mass flow rates are negligible in a mixture of LW and water and are very small in a mixture of NEMP. In our numerical results, the first term on the right-hand side of Eq. (36) mainly contributes to the mass flow rates because of the coefficient  $\rho_n^{(\text{eq})}$ , although the second term, with the coefficient 1/2, cannot be neglected altogether, in the presence of the preferential adsorption.

Driven by the pressure difference ( $\delta P \neq 0$  and  $\delta c_a = 0$ ) in the presence of the preferential adsorption, the total mass flow goes into the reservoir with smaller  $P$ . The term involving  $\mathcal{L}_{11}$  mainly contributes to the mass flow rates, which change slightly with  $\tau$  because  $\mathcal{L}_{11}$  depends on  $\psi^{(0)}$  only via  $\eta_s$ . The mass fraction of the mixture convected per unit time,  $c_{\text{aR}}^{(\text{flux})}$ , deviates slightly from  $c_a^{(\text{eq})}$ , which is caused mainly by the term involving  $\mathcal{L}_{21}$ . Accordingly,

the mixture flowing out of the tube has larger density of the component adsorbed by the tube wall as  $\tau$  decreases. Driven by the mass-fraction difference ( $\delta P = 0$  and  $\delta c_a \neq 0$ ) in the presence of the preferential adsorption, the total mass flow goes into the reservoir where the component adsorbed by the tube wall is less concentrated. The magnitude of the total mass flow rate remarkably increases as  $\tau$  decreases, which arises from the increase of the magnitude of  $\mathcal{L}_{12}$ . The mass flow rates of the components are subsidiarily affected by  $\mathcal{L}_{22}$ . A part of this component,  $\mathcal{L}_{22v}$ , increases remarkably as  $\tau$  decreases, while the rest,  $\mathcal{L}_{22d}$ , depending on  $\psi^{(0)}$  only via  $\Lambda$ , is rather insensitive to  $\tau$ .

The magnitudes of  $\mathcal{L}_{12} = \mathcal{L}_{21}$  and  $\mathcal{L}_{22v}$ , depending on  $\psi^{(0)}$  explicitly, increase with decreasing  $\tau$  because of the increasing magnitude of  $\psi^{(0)}$  in the presence of the preferential adsorption. The composition  $\varphi^{(0)}$  is related with the correlation length,  $\xi$ . Thus, assuming homogeneous  $\xi$  can give a very different composition profile, which yields a very different values of  $\mathcal{L}_{12} = \mathcal{L}_{21}$  and  $\mathcal{L}_{22}$ , as mentioned in Sect.V A 2. We take into account the inhomogeneity to calculate the components of  $\mathcal{L}$  by using the renormalized local functional theory[12].

In the absence of the preferential adsorption, Eq. (12) is written as  $\nabla P$  to yield the usual Hagen-Poiseulle flow. In the presence, we instead use Eq. (40) and (41) because of the inhomogeneity of the mass densities. This change in the reversible part of the pressure tensor makes  $\mathcal{L}_{12} = \mathcal{L}_{21}$  and  $\mathcal{L}_{22v}$  emergent in the presence of the preferential adsorption. In particular, the near-critical increase of the total mass flow rate in a flow driven by the mass-fraction difference gives a plain manifestation of the well-known change in the reversible part. As for the irreversible part, whether the preferential adsorption is present or not, Curie's principle prohibits the viscous stress and the diffusive flux from being linearly related with the gradient of a chemical potential and with the velocity gradient, respectively[23]. The prohibition can be also explained in terms of the difference in the parity with respect to the time-reversal symmetry between  $\mathbf{v}$  and  $\varphi$ [44].

Let us summarize the present study. We consider an isothermal transport of a binary fluid mixture in the homogeneous phase near the demixing critical point through the tube connecting two reservoirs. Our main results presuppose a cylindrical tube. In the numerical

calculations, the mixture is assumed to have the critical composition in the central region of the reservoir at the equilibrium. A flow can be driven by pressure difference and/or mass-fraction difference between the reservoirs. It is well expected that a flow driven by pressure difference convects a mixture with the mass-fraction modified by the preferential adsorption occurring between one mixture component and the tube wall. This cross effect is rather weak to the mass flow rates because it is included in the second term on the right-hand side of Eq. (36), and is linked via the reciprocal relation with the other cross effect. This cross effect enables a flow driven by a mass-fraction difference to have convective transport. This emerging effect raises the total mass flow rate remarkably as the critical point is approached, because it is included in the first term on the right-hand side of Eq. (36), which is usually much larger than the second term. The critical enhancement of the transport coefficients does not involved in these phenomena, because of the off-critical composition in the tube due to the preferential adsorption.

According to our results, the mass flow rates per a tube is the order of ng/s. Their magnitudes may become larger for sets of parameter values other than examined here. Furthermore, setting up several tubes in parallel may make the rates large enough in total to be measurable experimentally. Considering the significance of  $\varphi^{(0)}$  to the terms emergent in the presence of the preferential adsorption, the change in the mass flow rates may be more eminent when the capillary condensation[12] occurs in the tube. It is also of interest to study the mass flow rates caused by the temperature difference between the reservoirs. For this study, we should extend the renormalized local functional theory so that it can describe the equilibrium density of the internal energy of the mixture. We assume the tube to be cylindrical in deriving Eq. (27). Numerical results of the cross effects should be available for tubes with non-circular cross-sections[45]. In Appendix B, we show that our formulation is consistent with Onsager's reciprocal relation by using the no-slip boundary condition at the tube wall. It remains to be studied how this derivation for the consistency is extended when the condition is not valid in a sufficiently thin tube.

## Acknowledgements

The authors thank Prof. P.G. Wolynes for informing them of Ref. [25]. YF appreciates stimulating discussion with T. Iyori.

## Appendix A: Non-dissipative part of the stress tensor

As in the usual thermodynamics, we can derive the reversible part of the pressure tensor by considering the change of  $\mathcal{F}$  due to a infinitesimal quasistatic deformation of mixture[1, 13]. In this non-dissipative deformation, the chemical potentials  $\mu_a$  and  $\mu_b$  can be inhomogeneous, as in the magnetic system under an inhomogeneous magnetic field, which means that each locus in the mixture has each particle bath. Here, unlike in the text,  $V_{\text{tot}}$  is the deformable region occupied by the mixture,  $t$  is not the time but a parameter of deformation,  $\mathbf{v}$  is the displacement of fluid particle per unit  $t$ , and  $\mathbf{j}_n$  represents the flux to the particle bath. The last implies that  $\mathbf{j}_a + \mathbf{j}_b$  does not always vanish. Consider a small region,  $V_t$ , which co-moves with the deformation. This region is assumed to have the smallest volume that we can well define  $\mu_n$  and  $\Pi_{\text{rev}}$ , which can be regarded as homogeneous over this small region. Below, the repeated indices are summed up. The local equilibrium in the bulk gives

$$\frac{d}{dt} \int_{V_t} d\mathbf{r} f_{\text{bulk}} = \mu_n \frac{d}{dt} \int_{V_t} d\mathbf{r} \rho_n(\mathbf{r}, t) - \Pi_{\text{rev}} : \int_{\partial V_t} dA \mathbf{n}_{\partial V_t} \mathbf{v}, \quad (\text{A1})$$

where  $\Pi_{\text{rev}} : (\mathbf{n}_{\partial V_t} \mathbf{v})$  equals  $(\Pi_{\text{rev}})_{ij} (n_{\partial V_t})_j v_i$  in terms of the components with respect to the Cartesian coordinates. Equation (A1) yields

$$\frac{Df_{\text{bulk}}}{Dt} + f_{\text{bulk}} \nabla \cdot \mathbf{v} = -\mu_n \nabla \cdot \mathbf{j}_n - \Pi_{\text{rev}} : (\nabla \mathbf{v}) \quad (\text{A2})$$

with the aid of Eq. (14). Here,  $D/Dt$  represents the Lagrangian “time-derivative”. Because  $V_{\text{tot}}$  also co-moves with the deformation, we have

$$\frac{d\mathcal{F}}{dt} = - \int_{V_{\text{tot}}} d\mathbf{r} [\mu_n \nabla \cdot \mathbf{j}_n + \Pi_{\text{rev}} : (\nabla \mathbf{v})], \quad (\text{A3})$$

apart from a surface term. Here,  $\mu_n$  and  $\Pi_{\text{rev}}$  can depend on  $\mathbf{r}$ .

We below outline how Eqs. (9) and (11) are derived from Eq. (8). The Lagrangian “time-derivative” of  $f_{\text{bulk}}$  is found to be the sum of

$$\frac{\partial f_{\text{bulk}}}{\partial \rho} \frac{D\rho}{Dt} + \frac{\partial f_{\text{bulk}}}{\partial (\nabla \rho)} \cdot \nabla \left( \frac{D\rho}{Dt} \right) - \frac{\partial f_{\text{bulk}}}{\partial (\nabla \rho)} \cdot (\nabla \mathbf{v}) \cdot (\nabla \rho) \quad (\text{A4})$$

and the above with  $\rho$  replaced by  $\varphi$ . Substituting this result into the left-hand side of Eq. (A2), and integrating the result over  $V_{\text{tot}}$ , we can transform the bulk contribution to  $d\mathcal{F}/(dt)$  into the form of the right-hand side of Eq. (A3) with  $\mu_n$  and  $\Pi_{\text{rev}}$  given by Eqs. (9) and (11) apart from a new surface term, which is generated by the application of the divergence theorem. Below,  $\nabla_{\parallel} \cdot \mathbf{v}_{\parallel}$  indicates the divergence defined on  $\partial V_{\text{tot}}$  and  $H_m$  denotes the mean curvature of  $\partial V_{\text{tot}}$ . The latter is defined so that it is positive when the center of curvature lies on the side directed by  $\mathbf{n}_{\partial V_{\text{tot}}}$ . The surface term unwritten in Eq. (A3) is combined with the new surface term. With the aid of Eq. (19), we find the combination to yield the sum of

$$\int_{\partial V_{\text{tot}}} dA f_{\text{surf}} (\nabla_{\parallel} \cdot \mathbf{v}_{\parallel} - 2H_m \mathbf{v} \cdot \mathbf{n}_{\partial V_{\text{tot}}}) \quad (\text{A5})$$

and the surface integral of the terms involving the Lagrangian “time-derivatives” of the mass densities. We can use Eq. (14) to rewrite these derivatives in terms of  $\mathbf{j}_n$ . This flux should not exist at  $\partial V_{\text{tot}}$ , where the particle bath does not exist. This means that the coefficients of the Lagrangian “time-derivatives” should vanish, which leads to Eq. (19). This equation is thus shown to hold even in the dynamics[43]. Hence, the surface term unwritten on the right-hand side of Eq. (A3) is blackuced to Eq. (A5), which means that  $-f_{\text{surf}}$  works as a two-dimensional pressure in  $\partial V_{\text{tot}}$ . The force density  $2f_{\text{surf}} H_m \mathbf{n}_{\partial V_{\text{tot}}}$  yields the Laplace pressure, as discussed in Appendix A of Ref. [46].

The transport coefficients are introduced in relating the irreversible fluxes linearly with the thermodynamic forces;  $\eta_s$  relates the viscous stress with the rate-of-strain tensor and  $\Lambda$  relates the difference of the diffusion flux with that of the chemical potentials. The reversible parts of the hydrodynamic equations contain nonlinear terms, as shown in Eqs. (11) and (16). The sum of the first two terms on the right-hand side of Eq. (17) equals the sum of  $-\rho_n \nabla \mu_n$  over  $n = a$  and  $b$ . Each term is linked with the first term on the right-hand side of Eq. (14) via the reciprocal relation after the hydrodynamic equations are linearized, as shown in Ref. [47]. This represents the adequacy of the first two terms on the right-hand side of Eq. (17), and underlies the cross effects mentioned in the penultimate paragraph of

Sect. VI.

### Appendix B: Onsager's reciprocal relation

We consider two sets of flow fields, each being driven by the thermodynamic forces  $(-\delta P_k/T, -\delta\mu_k/T)$ , with  $k$  being i or ii. In the set labeled by  $k$ , the thermodynamic fluxes and a field in the tube are also indicated by the subscript  $k$ . Applying different ways of integration by parts to the volume integral of  $\eta_0 E_i^{(1)} : E_{ii}^{(1)}$  over the region of the tube, denoted by  $V_{\text{tube}}$ , we obtain

$$\int_{V_{\text{tube}}} d\mathbf{r} \mathbf{v}_{ii}^{(1)} \cdot \left[ \nabla \cdot \left( \eta_0 E_i^{(1)} \right) \right] = \int_{V_{\text{tube}}} d\mathbf{r} \mathbf{v}_i^{(1)} \cdot \left[ \nabla \cdot \left( \eta_0 E_{ii}^{(1)} \right) \right], \quad (\text{B1})$$

where we note that the no-slip boundary condition is imposed at the inner surface of the tube and that  $\nabla \cdot \mathbf{v}_k^{(1)}$  vanishes in the stationary laminar flow in the tube. Substituting Eq. (17) into Eq. (B1), we use Eq. (26) to find that

$$\frac{\delta P_i - \varphi_c \delta \mu_i}{\rho^{(\text{eq})} L_{\text{tube}}} \int_{S_{\text{tube}}} dA \rho^{(0)} v_{iiz}^{(1)} + \frac{\delta \mu_i}{L_{\text{tube}}} \int_{S_{\text{tube}}} dA \varphi^{(0)} v_{iiz}^{(1)} \quad (\text{B2})$$

equals the above equation with the subscripts  $i$  and  $ii$  exchanged. Putting  $\delta \mu_i$  and  $\delta P_{ii}$  equal to zero, we have

$$\mathcal{I}_{ii} \delta P_i = \mathcal{J}_i \delta \mu_{ii} \quad (\text{B3})$$

because  $j_{iz}$  vanishes. This means  $\mathcal{L}_{12} = \mathcal{L}_{21}$ , which leads to  $\mathcal{K}_{12} = \mathcal{K}_{21}$ . Note that this derivation of the reciprocal relations is valid even when  $\rho^{(0)}$  is inhomogeneous, unlike the one given in Ref. [26].

### Appendix C: Renormalized local functional theory

The mass densities of the mixture components have the probability densities in the fluctuation about the equilibrium. The effective Hamiltonian is defined so that the exponential of its negative is proportional to the probability density functional. It is usually assumed that the  $\psi$ -dependent part is of the Landau-Ginzburg-Wilson type, or the  $\psi^4$  model, as a bare model for a mixture bulk. At the equilibrium near the critical point, the bare model gives almost the same probabilities, close to the maximum probability, to many composition profiles, which differ from each other only by details with length scales smaller than

the local correlation length, and thus remarkable composition fluctuations arise over these scales. Changing the way of counting profiles to neglect small differences between profiles, we can unify many profiles into much fewer profiles. That is, coarse-graining  $\psi$  up to the local correlation length enables us to regard the average profile as maximizing the resultant probability density functional, which is called renormalized local functional[12]. The  $\psi$ -dependent part of the coarse-grained effective Hamiltonian for a mixture bulk with  $\mu = 0$  is given by the volume integral of the sum of

$$\frac{1}{2}C_1\xi_0^{-2}\omega^{\gamma-1}\tau\psi^2 + \frac{1}{12}C_1C_2\xi_0^{-2}\omega^{\gamma-2\beta}\psi^4 \quad (\text{C1})$$

and

$$\frac{1}{2}C_1\omega^{-\eta\nu}|\nabla\psi|^2 . \quad (\text{C2})$$

over  $V_{\text{tot}}$ . Here,  $C_1$  is a positive nonuniversal constant, and  $C_2$  is given by

$$C_2 = 3u^*C_1\xi_0 , \quad (\text{C3})$$

where  $u^*$  denotes the scaled coupling constant at the Wilson-Fisher fixed point. We have  $u^* = 2\pi^2/9$  in the three dimensions at the one loop order. The quantity  $\omega$ , defined by Eq. (42), satisfies a self-consistent condition,

$$\omega = \tau + C_2\omega^{1-2\beta}\psi^2 , \quad (\text{C4})$$

which comes because the mean-field approximation is valid after coarse-graining up to  $\xi$ . We can use Eq. (C4) to calculate  $\xi$  at  $\mathbf{r}$  from  $\tau$  and  $\psi(\mathbf{r})$ . A large value of  $\xi$  at a point would not imply the correlation length at the point if the values are small near the point. Thus, the resolution of the coarse-grained theory in a region would not be determined by  $\xi$  at a point in the region. The logarithm of the probability density is proportional to Eq. (18) divided by  $-k_B T$ . Thus, we can identify the difference of  $(\mu_-)_c\varphi$  subtracted from  $f_-(\psi)$ , appearing in Eq. (37), with the product of  $k_B T$  and Eq. (C1), and identify  $M_-(\psi)$  with  $k_B T C_1 \omega^{-\eta\nu}$  because of Eq. (C2).

#### Appendix D: Evaluation of $C_2$

The linear relationship between the refractive index and the volume fraction in a mixture of LW is shown in Fig. 2 of Ref. [48]. Using the three values shown by the circles in this



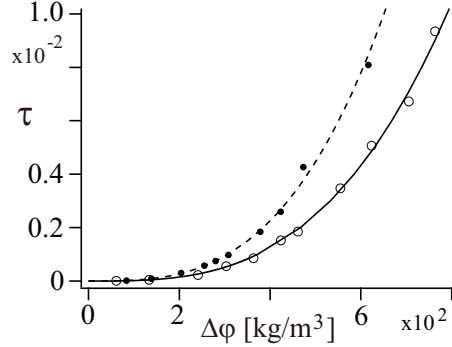


FIG. 15: Relationship between  $\tau$  and the difference in  $\varphi$  between coexistence phases in the mixture. Open and solid circles are replots of data in Ref. [48] for a mixture of LW and data in Ref. [49] for a mixture of NEMP, respectively. Solid and dashed curves are obtained by the curve-fits of twice the value of Eq. (3.3) of Ref. [12] to these sets of data, respectively.

figure and the index of the pure water, 1.330, we obtain the fitted line with the slope of  $1.77 \times 10^{-1}$ . Reference [48] also shows the refractive indices of the coexistent two phases above the lower consolute temperature. Converting the difference of the indices into that of  $\varphi$  with the aid of the values of  $\bar{v}_n^{(\text{eq})}$  mentioned in the text, we plot the relationship between the latter difference ( $\Delta\varphi$ ) and  $\tau$  in Fig. 15. The coexistence curve for  $\mu = 0$  is given by Eqs. (3.3) and (3.23) of Ref. [12], and the data are approximately regarded as obtained for  $\mu = 0$ . Curve-fit to the data of Ref. [48] yields  $C_2 = 7.14 \times 10^{-7} \text{ m}^6/\text{kg}^2$  for a mixture of LW. As for a mixture of NEMP, we obtain the relationship between  $\Delta\varphi$  and  $\tau$  from data (Run A) of Ref. [49] and find  $C_2 = 1.05 \times 10^{-6} \text{ m}^6/\text{kg}^2$  (Fig. 15).

### Appendix E: Transport coefficients

We first mention the previous studies of the dynamic renormalization group calculation for the mixture bulk[50–52]. The  $\psi^4$  model is used as a bare model for an incompressible mixture having vanishing average of  $\psi$ . In this mixture,  $\xi$  is homogeneously equal to  $\xi_0\tau^{-\nu}$ . The interdiffusion coefficient equals  $\Lambda$  divided by the osmotic susceptibility, given by  $1/f''(0)$ , and is found to equal  $\lambda^*k_o^{4-z_\psi}\xi^{2-z_\psi}$  in a near-critical mixture. Here,  $\lambda^*$  is a constant determined at the fixed point of the renormalization group flow starting from a bare model having  $k_o$  as the cutoff wavenumber;  $1/k_o$  is a microscopic length scale. With  $z_\eta$  denoting  $z_\psi - d$ , where  $d$  is the spatial dimensions, the singular part of the viscosity, denoted by  $\eta_{\text{sing}}$ , becomes given

by  $\eta^*(k_o\xi)^{z_\eta}$  as the critical point is approached. Here,  $\eta^*$  is a constant determined at the fixed point and is not  $\eta_*$  defined in the text. In a near-critical mixture, we thus have

$$\Lambda = \frac{\lambda^*(k_o\xi)^{4-z_\psi}}{f''_-(0)\xi^2} = \frac{Rk_B T_c}{f''_-(0)\xi^{d-2}\eta_{\text{sing}}}, \quad (\text{E1})$$

where  $f''_-(0)$  equals  $k_B T C_1 \tau^\gamma \xi_0^{-2}$  and  $R$  is a universal constant called Kawasaki amplitude. The second equality above comes from the definition of this constant. Below,  $d$  is put equal to be three, as in the text. From the experimental data of  $2\Lambda M_-/\xi^4$  on the critical isochore[36, 40], the value of  $2\lambda^* k_o^{4-z_\psi} \xi_0^{-z_\psi}$  is  $2.5 \times 10^{10} \text{ s}^{-1}$  for a mixture of LW, and  $1.23 \times 10^{11} \text{ s}^{-1}$  for a mixture of NEMP. Applying these values in the first equality of Eq. (E1), we obtain  $\Lambda_* = 2.19 \times 10^{-9} \text{ kg}\cdot\text{s}/\text{m}^3$  and  $2.78 \times 10^{-8} \text{ kg}\cdot\text{s}/\text{m}^3$  for respective mixtures.

The product  $\nu z_\eta$  is measurably to be around 0.042[53, 54], which leads to  $z_\psi = 3.067$ . Because of the weak singularity, the viscosity at the critical composition can be well described in the form of multiplicative anomaly as[55, 56]

$$A_\eta \exp\left[\frac{B_\eta}{T - T_\eta}\right] \exp[z_\eta H(\tau, q_D, q_C)], \quad (\text{E2})$$

where  $H(\tau, q_D, q_C)$  is the crossover function with  $q_D$  and  $q_C$  being wavenumber parameters. It is defined at Eq. (2.18) of Ref. [57], approaches zero as  $\xi$  tends to zero, and approaches the sum of  $\ln \xi$  and a constant as  $q_C \xi$  is larger. Thus,  $\eta_{\text{sing}}$  is given by Eq. (E2) with  $T - T_\eta$  being replaced by  $T_c - T_\eta$ . This leads to  $\eta_{\text{sing}} \propto \xi^{z_\eta}$  for  $T \approx T_c$ , as it should do. We approximate  $\eta_*$  to be Eq. (E2) at  $T = T_*$ , where  $T_*$  is  $T$  at  $\tau = \tau_*$ , considering that  $\tau_*$  is very small. The calculation result for  $\Lambda$  in the mode coupling theory[3], agrees with the right-hand side of Eq. (E1) if  $R$  is put equal to  $1/(6\pi)$  and if  $z_\eta$  is regarded as zero. In Ref. [50],  $R$  is approximately estimated to be  $1/(5\pi)$ .

In Eqs. (16) and (17), we need the values of the transport coefficients for off-critical compositions. As in Eq. (4.11) of Ref. [16], we obtain the value of  $\Lambda_0$  by regarding  $\xi$  as given by Eq. (42) and replacing  $f''_-(0)$  by  $f''_-(\psi^{(0)})$  in Eq. (E1). This definition yields Eq. (53) with right-hand side multiplied by a factor  $T_*/T$ . We neglect the factor, which is close to unity in the range of  $\tau$  examined. The fraction in the last term in the last entry of Eq. (57) is originally the left-hand side of Eq. (E3) below. We use the definitions to obtain

$$\frac{2\pi r_{\text{tube}}^2}{L_{\text{tube}}} \times \frac{\Lambda_* \mu_*}{\mathcal{I}_* \psi_*} = \frac{48 T_c u^* R}{T_*}. \quad (\text{E3})$$

Approximating  $T_*$  to be  $T_c$  and using  $R = 1/(6\pi)$ , we obtain the fraction in Eq. (57).

We below mention a fitting function of  $\eta_s$  for off-critical compositions. As a fitting function to the data out of the peak in Figs. 3(a) and 11(a), we use

$$A_\eta \exp \left[ \frac{B_\eta}{T - T_\eta} \right] + G(c_a - c_{ac}) , \quad (\text{E4})$$

where  $G$  is a quartic function vanishing at  $c_a = c_{ac}$ [57]. The difference in the parentheses in the last term above represents the variable of  $G$ . The dependence of the four coefficients of the quartic function on  $\tau$  are estimated from curve-fittings. Subtracting the background viscosity given by Eq. (E4) from the data, we fit the difference to[58]

$$A_\eta \exp \left[ \frac{B_\eta}{T - T_\eta} \right] \{ \exp [z_\eta H(\tau, q_D, q_C)] - 1 \} \exp [-\zeta (c_a - c_{ac})^2] , \quad (\text{E5})$$

where  $\zeta$  is a positive constant to be estimated from the data in the peak. Thus, we can obtain the viscosity as a function of  $\tau$  and  $c_a$ , which can be converted into a function of  $\tau$  and  $\varphi$  with the aid of

$$c_a = \frac{1}{2} + \frac{(\bar{v}_a^{(\text{eq})} + \bar{v}_b^{(\text{eq})}) \varphi}{4 - 2(\bar{v}_a^{(\text{eq})} - \bar{v}_b^{(\text{eq})}) \varphi} . \quad (\text{E6})$$

This is obtained from Eq. (3) with the aid of  $\varphi = \rho(2c_a - 1)$ . The function  $\eta_0$  is obtained by replacing  $\varphi$  with  $\psi^{(0)}(r) + \varphi_c$ . For the linear phenomenological equations, we need not consider the suppression of the enhancement due to a strong shear[51, 59, 60].

For a mixture of LW on a critical isochore immediately below the lower consolute temperature,  $A_\eta$ ,  $B_\eta$ ,  $T_\eta$ ,  $q_C$ , and  $q_D$  are estimated to be  $1.4 \times 10^{-7}$  Pa·s,  $2.916 \times 10^3$  K, 0.2 K,  $10^{11} \text{ m}^{-1}$ , and  $10^9 \text{ m}^{-1}$ , respectively[36]. Using the experimental data for off-critical compositions in Ref. [37, 38], we find  $5.37 + 58.9\tau$ ,  $1.34 + 68.3\tau$ ,  $-13.1 + 71.4\tau$ , and  $-3.29 - 683\tau$  mPa·s as the coefficients of the linear, quadratic, cubic, and quartic term of  $G$ , respectively. From the data of the circles in the peak in Fig. 3, we obtain  $\zeta = 2.60 \times 10^2$ . The results of the curve-fits are shown in Fig. 3(a). Equation (E2) with  $q_C = 1.3 \times 10^9 \text{ m}^{-1}$  and  $q_D = 3.2 \times 10^8 \text{ m}^{-1}$  is used for a mixture of NEMP on a critical isochore immediately above the upper consolute temperature in Ref. [40]. We use the dashed line in Fig. 1 of this reference as the first term on the right-hand side of Eq. (E4). The experimental data in Ref. [41] include the values of  $\eta_s$  for off-critical compositions. However, the data at the critical composition are slightly

different from those calculated from Eq. (E2) with the values of  $q_C$  and  $q_D$  mentioned above. Thus, so that they agree with each other, we shift the data for each value of  $\tau$  in Ref. [41]. The sets of data at  $\tau = 1.47 \times 10^{-4}$ ,  $1.82 \times 10^{-3}$ , and  $1.19 \times 10^{-2}$  are respectively raised by  $8.60 \times 10^{-3}$ ,  $4.80 \times 10^{-3}$ , and  $1.25 \times 10^{-2}$  mPa·s. The modified data are shown in Fig. 11(a). Then, we obtain  $0.303 - 2.74\tau$ ,  $-0.812 + 32.8\tau$ ,  $0.212 + 13.5\tau$ , and  $5.28 - 159\tau$  mPa·s as the coefficients of the linear, quadratic, cubic, and quartic term of  $G$ , respectively and obtain  $\zeta = 2.66 \times 10^2$ . The results of the curve-fits are shown in Fig. 11(a).

### Appendix F: Gaussian model

We assume that Eq. (C4) can be approximated to be  $w \approx \tau$ . This is combined with Eqs. (C1) and (C2) to give  $f_-(\psi) - \mu_c \varphi = M_- \psi^2 / (2\xi^2)$  approximately, with the  $\psi^4$  term being neglected. We obtain the Gaussian model by approximating  $M_-$  to be  $k_B T C_1$  furthermore. Applying these approximate expressions to Eqs. (38) and (39), we find the equilibrium profile in the cylindrical tube to be

$$\psi_G^{(0)}(r) = \frac{h\xi I_0(r/\xi)}{M_- I_1(r_{\text{tube}}/\xi)}, \quad (\text{F1})$$

where  $I_0$  and  $I_1$  denote modified Bessel functions. Although the correlation length is given by  $\xi_0 \tau^{-0.5}$  in the Gaussian model, we use  $\xi = \xi_0 \tau^{-\nu}$  homogeneously to obtain a better approximation and obtain the dotted curve in Fig. 4(a). In harmony with this approximation, we assume the transport coefficients to take the values for the critical composition anywhere. We use Eq. (E2) as  $\eta_s$  homogeneously, which makes  $\hat{\mathcal{L}}_{11}$  for a mixture of LW the same as given by the symbol + in Fig. 5(a). To calculate  $\mathcal{L}_{22d}$ , we homogeneously use

$$\Lambda = 1.25 \times 10^{10} \text{s}^{-1} \times \frac{\xi_0^4 \tau^{\nu(z_\psi + \eta - 4)}}{k_B T C_1}, \quad (\text{F2})$$

considering Eq. (E1) and the statement below Eq. (E2).

- 
- [1] R. Okamoto, Y. Fujitani, and S. Komura, "Drag coefficient of a rigid spherical particle in a near-critical binary fluid mixture," *J. Phys. Soc. Jpn* **82**, 084003 (2013).
- [2] A. Furukawa, A. Gambassi, S. Dietrich, and H. Tanaka, "Nonequilibrium critical Casimir effect in binary fluids," *Phys. Rev. Lett.* **111**, 055701 (2013).

- [3] K. Kawasaki, "Kinetic equations and time correlation functions of critical fluctuations," *Ann. Phys. (N.Y.)* **61**, 1 (1970)
- [4] T. Ohta, "Selfconsistent calculation of dynamic critical exponents for classical liquid," *Prog. Theor. Phys.* **54**, 1566 (1975).
- [5] H. Tanaka, "Interplay between wetting and phase separation in binary fluid mixtures: roles of hydrodynamics," *J. Phys., Condensed Matter* **13**, 4637-4674 (2001).
- [6] J. W. Cahn, "Critical point wetting," *J. Chem. Phys.* **66**, 3667 (1977).
- [7] D. Beysens, and D. Estève, "Adsorption phenomena at the surface of silica spheres in a binary liquid mixture," *Phys. Rev. Lett.* **54**, 2123 (1985).
- [8] D. Beysens and S. Leibler, "Observation of an anomalous adsorption in a critical binary mixture," *J. Physique Lett.* **43**, 133-136 (1982).
- [9] D. Bonn and D. Ross, "Wetting transitions," *Rep. Prog. Phys.* **64** 1085-1163 (2001).
- [10] M. N. Binder, *Phase Transitions and Critical Phenomena VIIIIV*, Critical behavior at surfaces. (Academic, London, 1983).
- [11] M. E. Fisher, and H. Au-Yang, "Critical wall perturbations and a local free energy functional," *Physica A* **101**, 255 (1980).
- [12] R. Okamoto and A. Onuki, "Casimir amplitude and capillary condensation of near-critical binary fluids between parallel plates: Renormalized functional theory," *J. Chem. Phys.* **136**, 114704 (2012).
- [13] A. Onuki, *Phase Transition Dynamics* (Cambridge University Press, 2002), Chap. 6.1.2.
- [14] S. Yabunaka, R. Okamoto, and A. Onuki, "Dynamics in bridging and aggregation of two colloidal particles in a near-critical binary mixture," *Soft Matter* **11**, 5738 (2015).
- [15] Y. Fujitani, "Undulation amplitude of a fluid membrane in a near-critical binary fluid mixture calculated beyond the Gaussian model supposing weak preferential attraction," *J. Phys. Soc. Jpn.* **86** 044602 (2017).
- [16] S. Yabunaka and Y. Fujitani, "Drag coefficient of a rigid spherical particle in a near-critical binary fluid mixture, beyond the regime of the Gaussian model," *J. Fluid Mech.* **886** A2 (2020).
- [17] L. Bocquet and E. Charlaix, "Nanofluidics, from bulk to interfaces," *Chem. Soc. Rev.* **39**, 1073-1095 (2010).
- [18] G. M. Whitesides, "The origins and the future of microfluidics," *Nature* **442**, 368-373 (2006).

- [19] M. D. Graham, "Fluid Dynamics of Dissolved Polymer Molecules in Confined Geometries," *Ann. Rev. Fluid Mech.* **43**, 273-298 (2011).
- [20] Y. Uematsu and T. Araki, "Electro-osmotic flow of semidilute polyelectrolyte solutions," *J. Chem. Phys.* **139**, 094901 (2013).
- [21] T. Yu, J. Zhou, and M. Doi, "Capillary imbibition in a square tube," *Soft Mat.* **14**, 9263 (2018).
- [22] E. Brunet and A. Adjari, "Generalized Onsager relations for electrokinetic effects in anisotropic and heterogeneous geometries", *Phys. Rev. E* **69**, 016306 (2004).
- [23] S. R. de Groot and G. Mazur, *Non-equilibrium thermodynamics*, (Dover, New York, 1984). Sect. IV and Chap. XV.
- [24] S. Samin and R. van Roij, "Interplay between adsorption and hydrodynamics in nanomechanics: Towards tunable membranes," *Phys. Rev. Lett.* **118**, 014502 (2017).
- [25] P. G. Wolynes, "Osmotic effects near the critical point," *J. Phys. Chem* **80**, 1570-1572 (1976).
- [26] X. Xu and T. Qian, "Generalized Lorentz reciprocal theorem in complex fluids and in non-isothermal systems," *J. Phys.: Condens. Matter* **31**, 475101 (2019).
- [27] L. Onsager, "Reciprocal relations in irreversible processes I," *Phys. Rev.* **37**, 405 (1941).
- [28] L. Onsager, "Reciprocal relations in irreversible processes II," *Phys. Rev.* **37**, 2265 (1941).
- [29] A. J. Bray and M. A. Moore, "Critical behaviour of semi-infinite systems," *J. Phys. A: Math. Gen.* **10**, 1927-1962 (1977).
- [30] H. W. Diehl, *Phase Transition and Critical Phenomena X*, Field theoretical approach to critical behavior at surfaces. (Academic, London, 1986).
- [31] H. W. Diehl, "The theory of boundary critical phenomena," *Int. J. Mod. Phys. B* **11**, 3503-3523 (1997).
- [32] P. G. de Gennes, "Physique des surfaces et des interfaces - Suspensions colloïdales dans un mélange binaire critique," *C. R. Acad. Sci. II* **292**, 701 (1981).
- [33] R. Okamoto and A. Onuki, "Attractive interaction and bridging transition between neutral colloidal particles due to preferential adsorption in a near-critical binary mixture," *Phys. Rev. E* **88**, 022309 (2013).
- [34] S. Yabunaka and A. Onuki, "Critical adsorption profiles around a sphere and a cylinder in a fluid at criticality: Local functional theory," *Phys. Rev. E* **96**, 032127 (2017).
- [35] A. Pelissetto and E. Vicari, "Critical phenomena and renormalization-group theory,"

- Phys. Rep. **368**, 549 (2002).
- [36] S. Z. Mirzaev, R. Behrends, T. Heimburg, J. Haller, and U. Kaatzke, "Critical behavior of 2,6-dimethylpyridine-water: Measurements of specific heat, dynamic light scattering, and shear viscosity," J. Chem. Phys. **124** 144517 (2006).
- [37] A. Stein, S. J. Davidson, J. C. Allegra, and G. F. Allen, "Tracer Diffusion and Shear Viscosity for the System 2,6-Lutidine-Water near the Lower Critical Point," J. Chem. Phys. **56** 6164 (1972).
- [38] C. A. Grattoni, R. A. Dawe, C. Y. Seah, and J. D. Gray, "Lower Critical Solution Coexistence Curve and Physical Properties (Density, Viscosity, Surface Tension, and Interfacial Tension) of 2,6-Lutidine + Water," Chem. Eng. Data, **38**, 516-519 (1993).
- [39] Y. Jayalakshmi, J. S. Van Duijneveldt, and D. Beysens, "Behavior of density and refractive index in mixtures of 2,6-lutidine and water," J. Chem. Phys. **100** 604-609 (1994).
- [40] I. Iwanowski, K. Leluk, M. Rudowski, and U. Kaatzke, "Critical dynamics of the binary system nitroethane/3-methylpentane: Relaxation rate and scaling function," J. Phys. Chem. A **110**, 4313 (2006).
- [41] H. M. Leister, J. C. Allegra, and G. F. Allen, "Tracer diffusion and shear viscosity in the liquid-liquid critical region," J. Chem. Phys. **51** 3701 (1969).
- [42] J. Reeder, T. E. Block, and C. M. Knobler, "Excess volumes of nitroethane + 3-methylpentane," J. Chem. Thermodyn. **8**, 133 (1976).
- [43] H. W. Diehl and H. K. Janssen, "Boundary conditions for field theory of dynamic critical behavior in semi-infinite systems with conserved order parameter," Phys. Rev. A **45**, 7145 (1992).
- [44] C. W. Gardiner, *Handbook of Stochastic Methods*, (Springer, Berlin, 1985). Sect. 5.3.
- [45] S. Shahsavari, A. Tamayol, E. Kjeang and M. Bahram, "Convective heat transfer in microchannels of noncircular cross sections: an analytical approach," ASMEJ. Heat Transfer **134**, 091701 (2012).
- [46] Y. Fujitani, "Effective viscosity of a near-critical binary fluid mixture with colloidal particles dispersed dilutely under weak shear," J. Phys. Soc. Jpn. **83**, 084401 (2014).
- [47] K. Miyazaki, D. Bedeaux, and K. Kitahara, "Nonequilibrium thermodynamics of multicomponent systems," Physica A **230**, 600 (1996).
- [48] K. To, "Coexistence curve exponent of a binary mixture with a high molecular weight poly-

- mer," *Phys. Rev. E.* **63**, 026108 (2001).
- [49] A. M. Wims, D. McIntyre, and F. Hynne, "Coexistence curve for 3-methylepentane-nitroethane near the critical point," *J. Chem. Phys.* **55** 4265 (1971).
- [50] E. D. Siggia, P.C. Hohenberg, and B. I. Halperin, "Renormalization-group treatment of the critical dynamics of the binary-fluid and gas-liquid transitions," *Phys. Rev. B* **13**, 2110-2123 (1976).
- [51] A Onuki and K. Kawasaki, "Nonequilibrium steady state of critical fluids under shear flow: a renormalization group approach," *Ann. Phys. (N.Y.)* **121**, 456-528 (1979).
- [52] R. Folk and G. Moser, "Critical dynamics: a field-theoretical approach," *J. Phys. A: Math. Gen.* **39**, R207-R313 (2006).
- [53] R. F. Berg and M. R. Moldover, "Critical exponent for the viscosity of four binary liquids," *J. Chem. Phys.* **89**, 3694-3704 (1989).
- [54] R. F. Berg and M. R. Moldover, "Critical exponent for viscosity," *Phys. Rev. A* **42**, 7183-7187 (1990).
- [55] T. Ohta, "Multiplicative renormalization of the anomalous shear viscosity in classical liquids," *J. Phys. C: Solid State Phys.* **10**, 791 (1977).
- [56] J. V. Sengers, "Transport properties near critical points," *Int. J. Thermophys.* **6**, 203-232 (1985).
- [57] J. K. Bhattacharjee, R. A. Ferrell, R. S. Basu, and J. V. Sengers, "Crossover function for the critical viscosity of a classical fluid," *Phys. Rev. A*, **24**, 1469 (1981). .
- [58] B. C. Tsai and D. McIntyre, "Shear viscosity of nitroethane-3-methylpentane in the critical region," *J. Chem. Phys.* **60**, 937 (1974).
- [59] A. Onuki, "Phase transitions of fluids in shear flow," *J. Phys, Condensed Matter* **9**, 6119-6157 (1997).
- [60] Y. Fujitani, "Suppression of viscosity enhancement around a Brownian particle in a near-critical binary fluid mixture," *J. Fluid Mech.* **907**, A21 (2021).